



## Supplementary Materials for

### **Metabolomics and mass spectrometry imaging reveal channeled de novo purine synthesis in cells**

Vidhi Pareek, Hua Tian, Nicholas Winograd\*, Stephen J. Benkovic\*

\*Corresponding author. Email: [sjb1@psu.edu](mailto:sjb1@psu.edu) (S.J.B.); [nxw@psu.edu](mailto:nxw@psu.edu) (N.W.)

Published 17 April 2020, *Science* **368**, 283 (2020)  
DOI: 10.1126/science.aaz6465

#### **This PDF file includes:**

Materials and Methods

Figs. S1 to S7

Tables S1 to S3

Captions for data S1 to S4

References

#### **Other supplementary material for this manuscript includes:**

Data S1 to S4 (Excel format)

## Materials and Methods

All the cell culture media components, RPMI, FBS, MEM, 1X PBS, were purchased from Corning Life Sciences, USA. HPLC grade water, methanol (MeOH), ethanol and chloroform were purchased from Fisher Scientific, USA. Source of other reagents used in the study are enlisted (table S1).

### **Description of the DNPB pathway and the rationale for colocalization with mitochondria:**

The step by step synthesis of the purine ring by the de novo pathway relies on numerous cofactors, coenzymes, and amino acid substrates. Glycolytic and TCA cycle intermediates are processed in conjunction with mitochondria to generate some of these, (fig. S1A). Assuming a homogenous distribution of all the enzymes, substrates and intermediates, the thermodynamic instability of 5-phosphoribosylamine (5-PRA), the product of the first committed step and an early intermediate of the DNPB pathway, would impede the pathway efficiency (2, 3). Evolution of a mechanism for co-clustering of the pathway enzymes into a functionally active purinosome metabolon that sequesters 5-PRA may be favored to achieve higher flux. Furthermore, germane to the reported localization of the purinosomes at the mitochondria is the requirement of Gly in the synthesis of glycinamide ribonucleotide (GAR) from 5-PRA by the enzyme GART; the requirement of formate in the synthesis of 10-formyltetrahydrofolate, a necessary cofactor for the transformylase activity of GARTase and AIRCARTase; and the requirement of aspartic acid in the synthesis of phosphoribosyl aminoimidazole succinocarboxamide (SAICAR) from phosphoribosyl aminoimidazole carboxylate (CAIR) by the SAICARsynthetase domain of the bi-functional enzyme PAICS and the synthesis of succinyl AMP (SAMP) from IMP by the enzyme ADSS. Inside the mitochondria, Serine (Ser), imported through the SFXN1 Ser transporter, produces Gly and formate by the operation of the one carbon mitochondrial cycle (14, 15, 17, 33, 34), and the cataplerosis of oxaloacetic acid produces aspartic acid (35, 36) (fig. S1A). Consequently, one hypothesis for the directed migration of purinosomes along the microtubules is to facilitate its access to mitochondrially generated metabolites.

### **HeLa cell culture and purine depletion:**

HeLa cells were maintained and propagated in purine rich media (P+, RPMI, with glutamine + 10% FBS) without any antibiotics. For purine depletion, the media was switched to RPMI + 5% dialyzed FBS and three passages were performed in the depleted media to obtain “P-” cells (7). FBS was extensively dialyzed against 0.15 M NaCl solution using 1 kDa cut-off membrane.

### **Labeling with $^{15}\text{N}$ Ser (Ser)/ $^{15}\text{N}_4$ hypoxanthine (Hypo):**

For estimating the salvage and de novo synthesis contribution in HeLa cells, the P+ and P- HeLa cells were grown in 100 mm culture dishes and at 80-90% confluency, cells were washed and metabolomic estimation was done by LC/MS on the 80% MeOH extracted metabolites. Alternately, the media was changed to MEM (with glutamine and 5% dialyzed FBS) with one of the following combinations of additives for purine enriched (P+) cells- a) 60  $\mu\text{M}$  unlabeled Hypo and 60  $\mu\text{M}$   $^{15}\text{N}$  Ser, or b) 60  $\mu\text{M}$   $^{15}\text{N}_4$  Hypo and 60  $\mu\text{M}$  unlabeled Ser; and purine depleted (P-) cells- 60  $\mu\text{M}$   $^{15}\text{N}$  Ser. Isotope uptake and incorporation was allowed for 4 hrs before metabolite extraction. Cell were washed gently with 1x PBS three times and 1.5 mL cold 80% methanol was

added covering the culture dish. Cell were harvested by scraping. The extract mix was spun for 30 mins at 4 °C, at 5700 x g and supernatant was collected and dried under N<sub>2</sub> gas flow and reconstituted in 30 µL 3% MeOH with 1 µM chlorpropamide (internal standard) and 10-15 µL of the extract was used for each LC-MS run.

### HPLC/ESI MS analysis:

Cell extracts were analyzed by LC/MS using a modified version of an ion pairing reversed phase negative ion electrospray ionization method (37). metabolites were separated on a Phenomenex (Torrance, CA, USA) Hydro-RP C18 column (100 × 2.1 mm, 3 µm particle size) using a water/MeOH gradient with tributylamine and acetic acid added to the aqueous mobile phase and analyzed by Exactive plus orbitrap mass spectrometer controlled by Xcalibur 2.2 software (all from Thermo Fisher Scientific, Waltham, MA). The HPLC column was maintained at 30 °C, and at flow rate of 200 µl/ min. Solvent A is 3% aqueous MeOH with 10 mM tributylamine and 15 mM acetic acid; solvent B is MeOH. The gradient used is 0 min, 0% B; 5 min, 20% B; 7.5 min, 20% B; 13 min, 55% B; 15.5 min, 95% B; 18.5 min, 95% B; 19 min, 0% B; and 25 min, 0% B. The Exactive Plus was operated in negative ion mode at maximum resolution (140,000) and scanned from *m/z* 72 to *m/z* 1000 for the first 90 sec and then from *m/z* 85 to *m/z* 1000 for the remainder of the chromatographic run. Standard metabolite solutions were run at 1 and 5 µM concentrations to obtain the standard retention time for each metabolite of interest under our experimental conditions (table S2). The expected difference in atomic mass ( $\Delta amu$ ) of the metabolites upon incorporation of different stable isotope labeled substrates is given (table S3).

### De novo purine biosynthesis (DNPB) model:

To understand and interpret the incorporation of labeled glycine (Gly) and formate in purine intermediates and end product nucleotides synthesized via the DNPB pathway, we developed a simple mathematical model. The model was based on the null hypothesis that DNPB operates in a completely diffusive manner with the pathway flux being determined by the thermodynamic and kinetic parameters of the involved enzymes and substrates and does not involve purinosome metabolon formation. The model is based on the following assumptions: homogenous level of mitochondria derived isotopically labeled substrates, <sup>13</sup>C<sub>2</sub>, <sup>15</sup>N Gly and <sup>13</sup>C formate in the cytosol; homogenous distribution of the DNPB enzymes in the cytosol; each of the 14 steps of the DNPB pathway (beginning from PRPP to AMP and GMP) are catalyzed independent of the preceding and succeeding reaction steps and thus each of the intermediates equilibrates with the total cytosolic pool (fig. S2A). The model can be mathematically formulated by assigning unlabeled and labeled Gly and formate fractions the values, (x) and (1-x), and (y) and (1-y), respectively, and treating the three steps at which Gly and formate get incorporated into the purine ring as mutually exclusive events (Fig. 1D and E). Isotope incorporation at each step is determined by the isotope labeled fractions of source substrates and the fractional abundance of different isotopomers produced at the three steps were calculated as follows:

1) Two isotopomers of GAR with the relative fractional abundances,  $(0) : (+3) = (x) : (1-x)$ ;

2) Four isotopomers of FGAR/SAICAR/AICAR with the relative fractional abundances,

$(0) : (+1) : (+3) : (+4) = (x*y) : (x*(1-y)) : ((1-x)*y) : ((1-x)*(1-y))$ , (Fig. 1F).

Also,  $[(0)+(1)] : [(+3)+(4)] = x : (1-x)$  and  $(0) : (+1) = (+3) : (+4) = y : (1-y)$ , (fig. S1B).

3) Six different isotopomers of FAICAR/IMP/AMP/GMP with relative fractional abundances  $(0) : (+1) : (+2) : (+3) : (+4) : (+5) = (x*y^2) : 2(x*y*(1-y)) : (x*(1-y)^2) : ((1-x)*y^2) : 2((1-x)*y*(1-y)) : ((1-x)*(1-y)^2)$ , (Fig. 1G).

Also,  $[(0)+(1)+(2)] : [(3)+(4)+(5)] = x : (1-x)$  and  $(0) : (1) : (2) = (3) : (4) : (5) = y^2 : 2y*(1-y) : (1-y)^2$ , (fig. S1C).

The two isotopomers produced from unlabeled ( $^{12}\text{C}$  Gly- 0) and labeled GAR ( $^{13}\text{C}_2$ ,  $^{15}\text{N}$  Gly- +3 Da) may be treated as independent pools which then generate the end nucleotides by either incorporating 0, 1 or 2  $^{13}\text{C}$  atoms derived from labeled formate. The model may be used both to predict the expected isotopomer distribution in the end product nucleotides or use the observed isotopomer distribution in the intermediates and the end nucleotides to back calculate the percentage labeling in the source substrates- Gly and formate, (fig. S1D). A model calculation using 20%  $^{13}\text{C}_2$ ,  $^{15}\text{N}$  Gly and  $^{13}\text{C}$  formate incorporation can be found in Supplementary Excel File 1.

In the absence of tools to study the purinosome complex in vitro, the model allowed us to make predictions that could be tested by performing in vivo pulse chase experiments. Also, since the model only uses isotope label percentages obtained from same experiment, it was particularly useful in overcoming the variations from different biological replicates and any experimental errors and the calculations could be performed on each individual dataset. The early intermediate GAR, produced from Gly incorporation, could not be estimated consistently due to instrument detection limits, thus we used the isotopomer distribution observed in the intermediates FGAR and SAICAR to calculate the respective isotope label fractions in Gly (1-x) and formate (1-y), (Fig. 1F). Now, using the isotopomer distribution in FGAR/SAICAR and the fraction labeled incorporation in formate, the expected isotopomer distribution in FAICAR was simulated, (Fig. 1G).

#### **Data processing and statistical analysis:**

For each experiment, the data from 3 or 4 biological replicates were collated to determine the mean and standard deviation. LC/MS results are visualized and processed using the Xcaliber Software, Thermo Scientific. The data is plotted, and statistical analysis performed using GraphPad Prism Version 8.2.1. The software Image Analyzer, Ionoptika Ltd, was used for post-acquisition calibration, analysis and visualization of GCIB-SIMS data.

#### **Calculating the newly synthesized pool of adenine and guanine nucleotides:**

When the unlabeled pool of a metabolite is completely replaced by the newly synthesized metabolite, the relative abundance of the different  $^{12}\text{C}$  Gly isotopomers (0: +1: +2) and that of the  $^{13}\text{C}_2$ ,  $^{15}\text{N}$  Gly isotopomers (+3: +4: +5) will be the same (fig. S2C). On the other hand, if these ratios are found to be different for a metabolite, that means the observed metabolite pool plausibly has a contribution from the DNPB flux during the experiment time, the existing unlabeled pools, and/or salvage synthesis. Though the +3, +4 and +5 species still can be attributed to the newly generated pool of nucleotides via DNPB.

The 0, +1 and +2 isotopomers of a nucleotide arise from  $^{12}\text{C}$  Gly containing species of the intermediates. Thus, IMP and all the nucleotides produced downstream of it, XMP, GMP, SAMP and IMP may potentially have contribution either from salvage synthesis and/or existent unlabeled pools in addition to DNPB. Therefore, the relative fractional abundances of the three isotopomers

are not only determined by the natural abundance of  $^{13}\text{C}$ ,  $^{15}\text{N}$ ,  $^2\text{H}$  and  $^{17}\text{O}$  but also the fraction of newly synthesized product. Under this scenario, the newly synthesized fraction can be computed as described below.

If the observed relative fraction of the three isotopomers  $+3:+4:+5 = 1:m:n$ , fraction of metabolite pool that has been replaced with the newly synthesized metabolite in the duration of the pulse chase experiment is “q”, and the expected relative fractions of  $(0:+1:+2)_e$  based on natural abundance =  $a:b:c$ . Then, the observed relative fractions of  $(0:+1:+2)_o$  would follow,  $(0)_o = [a*(1-q)] + (1*q)$ ;  $(+1)_o = [b*(1-q)] + (m*q)$ ;  $(+3)_o = [c*(1-q)] + (n*q)$ . Since “q” is the only unknown, it can be determined using the above set of equations. Since both unlabeled and labeled FGAR as well as unlabeled and labeled FAICAR are expected have equal  $^{13}\text{C}$  formate incorporation, the newly synthesized pool of the metabolite will have the same relative fractional abundance of  $0:+1:+2$  as  $+3:+4:+5$ , (Fig. 1E). The SAMP, GMP and AMP values shown in, respectively, were computed using the above method (fig. S2E and F, and Fig. 2C). Under our experimental conditions, very minor or no unlabeled isotopomer contribution was detected for IMP and XMP and thus no data processing was required.

### **In vivo isotope pulse chase experiments:**

Owing to the well-established route of Ser metabolism in HeLa cells, we hypothesized that labeled Ser would be taken up by mitochondria to produce labeled Gly and formate and under limiting availability of Ser, purinosomes located vicinal to mitochondria would show preferential isotope incorporation into the purinosome mediated DNPB intermediates and end nucleotides, reporting on the flux and enzymatic constitution of purinosomes (fig. S2A). In brief, P+ or P- HeLa cells were incubated in MEM with glutamine and 5% dFBS along with the desired concentration of labeled a)  $^{13}\text{C}_3$ ,  $^{15}\text{N}$  Ser, b)  $^{13}\text{C}_2$ ,  $^{15}\text{N}$  Gly and  $^{13}\text{C}$  Formate (to monitor de novo flux), or c)  $^{15}\text{N}_4$  Hypo. Metabolite extraction was performed as described in (7). Briefly, after 4 hrs of incubation with isotope labeled substrates, cells were washed three time with 1x PBS, and cold 80% MeOH was directly added to the culture dish to harvest cells by scraping. The cell extracts were dried under  $\text{N}_2$  gas flow and reconstituted in 30  $\mu\text{L}$  3% MeOH with 1  $\mu\text{M}$  chlorpropamide (internal standard) and 10-15  $\mu\text{L}$  of the extract was used for each LC/MS run. Data can be found in Supplementary Excel File 2.

The label incorporation in DNPB intermediates, end product nucleotides and other metabolites was quantified in the cell extracts using high resolution LC/MS. List of the metabolites reported in this work, along with their respective observed elution time, calculated  $m/z$  values and the molecular formulae (table S2). The isotope incorporation in DNPB pathway intermediates and end product nucleotides was determined at 30, 60 and 120  $\mu\text{M}$   $^{13}\text{C}_3$ ,  $^{15}\text{N}$  Ser and a low concentration of 30  $\mu\text{M}$  for a limited time pulse of 4 hrs was used for all further experiments, unless specified otherwise.  $^{13}\text{C}$  formate incorporation in formylmethionine and dTMP was used as the reporter of 10-formyl THF and 5,6-methylene THF production upon utilization of labeled Ser, (fig. S2B). We used isotopomer distribution difference between XMP and GMP to find the appropriate concentration in order to capture a non-equilibrium state of the pathway. As clear from the figure, while at 30 and 60  $\mu\text{M}$   $^{13}\text{C}_3$ ,  $^{15}\text{N}$  Ser, the fractional abundance of +3, +4 and +5 isotopomer of XMP and GMP was different, at 120  $\mu\text{M}$   $^{13}\text{C}_3$ ,  $^{15}\text{N}$  Ser the same was not true. Correspondingly, the formate enrichment difference between AMP and IMP was also non-significant at 120  $\mu\text{M}$  labeled Ser, (fig. S2M). In line with our hypothesis, in the 30  $\mu\text{M}$   $^{13}\text{C}_3$ ,  $^{15}\text{N}$  Ser labeling experiment, the isotopomer fraction analysis clearly shows that FGAR, SAICAR, IMP and XMP (Fig. 2B and fig. S2D) arise from the same source isotope enriched pool of Gly and formate, while, SAMP,

GMP, AMP (Fig. 2C and fig. S2E, and F) and all the downstream nucleotides (data not shown) arise from a higher isotope enriched pool of Gly and formate. Data can be found in Supplementary Excel File 2.

#### **Mycophenolic acid (MPA) treatment:**

To inhibit, both IMPDH1 and IMPDH2, MPA treatment was performed (38), at around 80-90% confluency. A 1000X stock solution of MPA was prepared in 100% MeOH. P- HeLa cells were washed and switched to MEM with glutamine (5% dFBS) with additional 30  $\mu\text{M}$   $^{13}\text{C}_3,^{15}\text{N}$  Ser. Three hrs post incubation, 10  $\mu\text{L}$  MeOH (as a control), or 30  $\mu\text{M}$  mycophenolic acid (#M3536, Sigma-Aldrich) were added to the media. After further incubation for one hr, cells were washed three times with 1x PBS, before proceeding with metabolite extraction with 80% MeOH, and LC/MS (fig. S2I, and Fig. 2F, and Supplementary Excel File 3).

#### **siRNA treatment for transient MTHFD2 knockdown:**

At around 60% confluency, P- HeLa cells grown in 100 mm culture dishes were washed with 1X PBS once and fresh RPMI (5% dFBS) added. siRNA treatment was performed as per manufacturer's recommendations. In brief, either ON-TARGET plus MTHFD2 siRNA smart pool (#L-009349-01, Dharmacon, USA) or ON\_TARGET plus, non-Target siRNA control pool (#D-001810-10, Dharmacon, USA) were mixed with RNAi MAX (#13778150, lipofectamine reagent). After mixing well, the master mix was allowed to stand at room temperature for 10 mins to allow the formation of RNA-lipid complexes and the mix was added to the culture dishes to achieve final siRNA concentration of 10 nM. To ensure that cell survival wasn't drastically affected due to lower formate production, after 8 hours of treatment, 60  $\mu\text{M}$  of unlabeled sodium formate was added to the growth media. 40 h post treatment, media was removed, cells were given a gentle wash with 1XPBS, and fresh RPMI (5% dFBS) and 120  $\mu\text{M}$  unlabeled sodium formate were added to the culture dishes. For isotope labeling, 48 h post treatment, media was replaced with MEM with glutamine (5% dFBS) and 30  $\mu\text{M}$   $^{13}\text{C}_3,^{15}\text{N}$  Ser. After further 4h incubation at 37 °C, cells were washed three times with 1x PBS and 1.5 ml cold 80% MeOH was added directly to the culture dish and cells were harvested by scraping. Metabolite extraction and LC/MS analysis was performed as described in the previous section and the metabolic abundance for AMP and AICAR was estimated (Fig. 2K, and Supplementary Excel File 3).

#### **Western blot analysis:**

After siRNA treatment, knockdown of the enzyme MTHFD2 was confirmed by Western blotting, (fig. S2K). The cell pellet obtained after metabolite extraction were reconstituted in 100  $\mu\text{L}$  buffer solution (6M urea, 2M thiourea in 4% CHAPS buffer) and incubated at room temperature (RT) for 1 hr, with vortexing every 15 mins. Lysate was centrifuged at 3000g for 20 mins and ~ 30  $\mu\text{L}$  of the soluble supernatant was drawn for sunning SDS-PAGE. For protein transfer to the PVDF membrane (#IPVH00010, Fisher Scientific), the semi-dry protocol was used as per the manufacturer's recommendations. Membrane was blocked using 5% w/v milk powder in TBST (0.1% Tween 20) for 2 hrs at RT. Anti-MTHFD2 primary antibody (rabbit anti-human antibody, #41377S, Cell Signaling) was reconstituted in the blocking buffer at 1:1000 dilution and overnight staining was allowed after which the membrane was washed thrice with TBST buffer at RT. Anti-rabbit HRP conjugated secondary antibody (#7074S, Cell Signaling) was diluted in the blocking buffer at 1:4000 dilution and the blot was stained for 3 hrs at RT. Following this, the membrane was washed 4 times with TBST the SuperSignal West Pico Plus Chemiluminescent substrate

(#34580, ThermoFisher Scientific). Protein migration on the SDS-PAGE was found to be affected due to the presence of urea and thiourea in the protein extract. Despite significant smearing of the gel, the knockdown of MTHFD2 upon target siRNA compared to the control siRNA treatment is evident (fig. S2K).

#### **Standard metabolite preparation:**

AMP sodium salt, ADP sodium salt, ATP sodium salt, GMP sodium salt, GDP sodium salt, GTP sodium salt, IMP, AICAR, SAICAR and glutathione were dissolved in HPLC grade water at a final concentration of 100  $\mu\text{M}$  for SIMS analysis or 1 and 5  $\mu\text{M}$  for HPLC/MS analysis (source details in table S1). For SIMS analysis, the cleaning procedure was conducted by consequent sonication of silicon wafers in chloroform, HPLC water, and ethanol for 15 mins each. The dried silicon wafers with analytes were plunge-frozen in liquid nitrogen ( $\text{LN}_2$ ) and analyzed in frozen-hydrated state. A 2  $\mu\text{L}$  drop of the analyte was spotted on a pre-cleaned silicon wafer and allowed to dry. Additionally, AMP (data not shown), AICAR (fig. S7C), and SAICAR monophosphate (data not shown) were dissolved in 0.1 M trehalose (#T9531, Sigma-Aldrich) solution at the concentrations 0.001, 0.01, 0.1, 1, 10  $\mu\text{M}$ . 10  $\mu\text{L}$  of the solution was used for spin-coating (6000 rpm) onto 5 mm  $\times$  5 mm pre-cleaned silicon wafer to form a uniform film (39). Intact molecular ions were observed for all the three analytes (fig. S3A, C and H).

#### **GCIB-SIMS analysis of metabolite standards:**

A DC beam buncher-ToF SIMS instrument and J105 3D Chemical Imager (Ionoptika, UK) were employed for all the measurement and imaging. The instrument was equipped with the new generation of GCIB as analyzing beam, harvesting the high spatial resolution ( $\sim 1 \mu\text{m}$ ) and high chemical sensitivity. It operates at high energy up to  $\sim 70 \text{ keV}$ , with the cluster size upto a few tens of thousands of  $\text{CO}_2$  gas molecules. Cluster is generated through supersonic expansion. High-pressure input gas passes through a de Laval nozzle, condensing into clusters at the exit due to rapid expansion and cooling of the gas. The neutral gas beam is then ionized by electron bombardment, before being focused through the column. A Wien filter allows for mass filtering, and a narrower distribution of cluster size ( $\pm 1000$ ). ToF measurements enable precise tuning of the clusters. In this study, the cluster beam, 70keV  $(\text{CO}_2)_n + (n=14,000)$  with a focus of 1  $\mu\text{m}$  was used to analyze the standards and the cell samples.

To determine the effective SIMS sensitivity for the intermediates, six parallel analyses were conducted on each standard sample at a primary ion fluence of  $1.7 \times 10^{13} \text{ ions} \cdot \text{cm}^{-2}$  using the  $>(\text{CO}_2)_{10,000}$  primary ion beam. Spectra were acquired by rastering the beam over an area of  $32 \times 32 \mu\text{m}^2$  with  $32 \times 32$  pixel. Because of the high count-rate associated with the most intense peaks, data are recorded in analog mode using a Fast Flight 2 (Ametek Technologies, Berwyn, PA) digitizing device. The signal intensity reported using the digitizer is proportional to the number of secondary ions hitting the detector. The intensities of molecular ion for each intermediate from mass window of  $\Delta m/z = 0.2$  were plotted as a function of the concentration. Signal dependence for AICAR is shown as an example. From the plot, the linear detection range and the detection limit can be determined. Even in the sub-micromolar concentration range, signal intensity shows a qualitative correlation with the concentration of the analyte (fig. S7C).

#### **Incorporation of $^{15}\text{N}$ Ser versus $^{13}\text{C}$ Gly in DNPB pathway intermediates and end product nucleotides:**

Multiply labeled  $^{13}\text{C}_3$ ,  $^{15}\text{N}$  Ser was not suitable for SIMS imaging experiments since it would subdivide each metabolite into six different isotopomers and the concentration of each may not be high enough to obtain significant signal from a  $1\ \mu\text{m} \times 1\ \mu\text{m} \times 350\text{-}400\ \text{nm}$  voxel. For assessing the utility singly labeled  $^{15}\text{N}$  Ser ( $60\ \mu\text{M}$ ) as the reporter for the channeled DNPB flux, we first performed labeling for 4 h and compared the labeling pattern with the control sample with  $^{13}\text{C}$  Gly ( $60\ \mu\text{M}$ ) label (fig. S5H and I). As described in the schematic, under high Gly availability, cell converts it to Ser by consuming the cytosolic one carbon units (5-methylene tetrahydrofolate), thus depleting the pool of 10-formyl tetrahydrofolate available for purine synthesis. This is expected to affect the channeled pathway flux and accumulation of AICAR intermediate. P- HeLa cells were grown in 100 mm culture dishes and after reaching 80-90% confluency, media was changed to MEM, 5% dialyzed FBS and  $^{15}\text{N}$  Ser or  $^{13}\text{C}$ Gly. Metabolite extraction was performed as described above and metabolites were analyzed using LC-MS. As expected, under Ser labeling, substantially low SAICAR and AICAR accumulation was observed compared to Gly labeling (fig. S5K). Interestingly, the adenine nucleotides, AMP and ATP, but not the guanine nucleotides showed significantly higher label incorporation in the Ser labeling experiment in comparison with the Gly labeling experiment (fig. S5J and L). It may be an outcome of the difference in partitioning of IMP into guanine and adenine nucleotides between diffusive (which shows clear bias towards guanine nucleotide synthesis) versus 'channeled' pathway. Thus, in the Gly labeling experiment, the lower total flux of DNPB may be balanced by higher partitioning in favor of the guanine nucleotides. These finding suggest that singly labeled  $^{15}\text{N}$  Ser can be used to monitor the 'channeled' DNPB pathway flux, thus we determined to perform MSI of HeLa cells with  $^{15}\text{N}$  Ser ( $60\ \mu\text{M}$ ) label incorporation and used  $^{13}\text{C}$  Gly as the control (Fig. 4G and I, and Supplementary Excel File 4).

#### **$^{13}\text{C}_3$ , $^{15}\text{N}$ Serine labeling for 14 hrs to confirm channeled DNPB:**

Before interpreting SIMS imaging results, we performed  $^{13}\text{C}_3$ ,  $^{15}\text{N}$  Ser labeling for 14hrs to confirm that the observations made for an early time point (4 hrs), hold true even after longer duration of isotope uptake. For this, we grew HeLa P- cells in a 100 mm culture dish for 14 hrs in MEM P- media supplemented with  $60\ \mu\text{M}$   $^{13}\text{C}_3$ ,  $^{15}\text{N}$  Ser. After this, metabolite extraction was performed as described above. Three independent biological replicates were performed and the newly synthesized isotopomer species (+3, +4 and +5 species) distribution in IMP and AMP was examined (fig. S6A, and Supplementary Excel File 4).

#### **Estimation of AICAR abundance per cell and per voxel volume in SIMS analysis:**

The metabolite extraction method we employed in our study does not allow dissociation of metabolites bound to the purinosome metabolon, thus allowing the estimation of intermediates that have either leaked from the complex or have been generated by the action of the diffused population of the DNPB enzymes. Thus, to estimate the total amounts of the pathway intermediate AICAR and end nucleotides, the dissociation of the purinosome metabolon is essential before metabolite extraction. We have previously reported the role of cytoskeletal elements in maintaining the purinosome assembly (10, 40), so we used limited treatment with trypsin to cause disruption of microtubular network to effect dissociation of purinosomes. HeLa cells were grown in purine depleted media and isotope labeled  $^{13}\text{C}_3$ ,  $^{15}\text{N}$  Ser incorporation was allowed for 14 hrs. Cells were trypsin treated for 2 mins to allow cytoskeleton disruption and purinosome dissociation. Trypsin action was quenched by adding pre-warmed RPMI with 5% dialyzed FBS. Cells were counted and after a wash with 3 mL 1x PBS, 1 mL 80% cold methanol was added to the cell pellet. Metabolite extraction was performed as described in the above. AICAR molecular abundance/ cell was



estimated using the slope value obtained for pure AICAR standards (fig. S6B). For obtaining the peak area corresponding to known AICAR amounts, the following AICAR solutions were prepared- 0.01, 0.1, 0.5, 1, 2, 5, and 10  $\mu\text{M}$ , and 10  $\mu\text{L}$  of each solution injected was for LC/MS. Four independent measurements were done, and linear regression was performed forcing Y intercept as zero.

Total HeLa cell volume has been estimated to be  $3700 \pm 1500 \mu\text{m}^3$  (41) and each voxel volume in a typical SIMS imaging experiment is  $0.35\text{-}0.4 \mu\text{m}^3$ . Thus, each voxel can be assumed to be  $1/10,000^{\text{th}}$  volume of a cell. From metabolomic estimation described above, the range of AICAR molecules was determined to be 750,000- 950,000/cell. Using the upper estimates of AICAR abundance, and assuming homogenous distribution of AICAR throughout the cell volume, AICAR abundance was calculated to be 100/voxel. For J105, Ionoptoka Ltd, a useful ion yield of  $1^{-4}\text{-}10^{-5}$  has been reported. Thus a biomolecular abundance of 10,000-100,000 molecules/voxel corresponds roughly to one ion/voxel detection (20). Thus, the above calculated AICAR abundance/voxel assuming a homogeneous molecular distribution is  $10^2 - 10^3$ -folds lower than the instrument detection limit.

### **HeLa cell culture for SIMS imaging:**

At around 80% confluency, cells were passaged and cultured onto 5 mm  $\times$  5 mm pre-cleaned silicon wafers by placing the wafer at the center of 10mm culture dishes with RPMI, 10% FBS (purine enriched; P+) or RPMI, 5% dialyzed FBS (purine depleted; P-). Cells were allowed to adhere to the silicon substrates for 8-10 hrs followed by media change to MEM (5% dialyzed FBS) with one of the following combinations of additives for 1) P- cells- a) 60  $\mu\text{M}$   $^{15}\text{N}$  Ser, or b) 60  $\mu\text{M}$   $^{13}\text{C}$  Gly; or 2) P+ cells- a) 60  $\mu\text{M}$  unlabeled adenine and 60  $\mu\text{M}$   $^{13}\text{C}$  Gly; b) 60  $\mu\text{M}$  unlabeled adenine and 60  $\mu\text{M}$   $^{15}\text{N}$  Ser; c) 60  $\mu\text{M}$   $^{15}\text{N}_4$  Hypo and 60  $\mu\text{M}$  unlabeled Gly (Fig. 3E to G). Label incorporation was allowed for 12-14 hrs at 37  $^\circ\text{C}$ . Simultaneously, cells were also grown in 100 cell culture dishes with labeled substrate incubation for 12 hrs and isotope incorporation was estimated with LC/MS (Fig. 3H). SIMS spectra after label incorporation were comparable to the isotope incorporation levels observed by exact estimation by LC/MS (Fig. 3F to H).

### **SIMS imaging of single HeLa cells:**

After 12-14 hrs incubation with isotope labeled compounds, cells were washed swiftly with 1 $\times$  PBS and with 0.05 M ammonia acetate 2 times, respectively, followed by removal of the extra liquid on the cell surface and plunge-freezing into liquid ethane. The samples were then loaded onto pre-cooled sample holder and transferred into the instrument under liquid  $\text{N}_2$  and with the protection of liquid  $\text{N}_2$  gas. The stages in the instrument were cooled down to 90 K before transferring the samples (39).

For SIMS imaging, the frozen hydrated cells were transferred to a pre-cooled copper stage at  $\sim 90$  K and cells were imaged with a finely focused 70 keV  $(\text{CO}_2)_n^+$  ( $n=14,000$ ) cluster beam. Continuous depth profiling was performed to reveal 3-dimensional chemical distribution. Because of the low damage by the cluster beam, we can afford to interrogate the cell surface continuously with just one beam, realizing the simultaneous sputtering and imaging acquisition without sacrificing the depth information. The beam was rastered pixel by pixel through the analyzed area and the cycle was repeated. Each cycle had the beam dose of  $1.7 \times 10^{13}$  ions $\cdot\text{cm}^{-2}$  over an area of  $256 \times 256 \mu\text{m}^2$  with  $265 \times 265$  pixel analyzed field/sample. The spectrum of each pixel is recorded against the coordinates for the reconstruction of chemical map. Most cells in the analyzed area

would be consumed after 15 cycles, which indicates approx. ~350-400 nm material from the cell was removed by each cycle (Fig. 3C).

### **Cryo- scanning electron microscopy:**

We performed cryo-scanning variable pressure, field emission scanning electron microscopy (SEM) (Zeiss SIGMA VP-FESEM), with a beam energy of 1 keV on flash frozen HeLa cells cultured under P+ RPMI (10% FBS) and P- (5% dFBS) to verify that cell morphology and integrity of remained unperturbed. HeLa cells were prepared identical to SIMS measurement, cultured on Si wafer, washed with 0.15 M ammonium formate solution followed by plunge freezing into liquid nitrogen. The samples were then transferred to a pre-cooled stage at 100 K for SEM characterization (fig. S5A to C).

### **Analysis of cellular morphology after GCIB-SIMS imaging:**

After post-data acquisition-calibration (fig. S4), the membrane lipids, represented by PI (38:4) at  $m/z$  885.55 and the fatty acids fragments at  $m/z$  255.25 and 283.25 (fig. S5G) are well retained in cellular body, with a width of approx. 40- 60  $\mu\text{m}$ . The purine base Hypo at  $m/z$  135.03 (fig. S5D) was also well within cells with a homogenous distribution (fig. S5F), with no sign of leaking out. In 3<sup>rd</sup> and 4<sup>th</sup> layers, the cell membrane components at  $m/z$  281.25+283.26 show a central low concentration region (fig. S5G), while Hypo (fig. S5D to F), and all other cytosolic analytes showed homogenous spread (data not shown). Thus, a line scan with these analytes in the first layer provides an estimate of the overall cell size (fig. S5E). The first 3 layers are primarily constituted by cytoplasm, where the purine de novo biosynthesis occurs. Therefore, only the first 2- 4 layers of cell scan were processed to statistically count the signal of the metabolites of interest, AICAR, AMP, ATP and GTP.

### **SIMS data processing:**

Post- acquisition calibration was applied to all SIMS spectra using internal standards before image generation and statistical analysis. Specifically, phosphoinositol, PI (38:4) at  $m/z$  885.54928, its intense fragments at  $m/z$  419.25624 and  $m/z$  283.26369 were used for 3-point calibration to achieve mass accuracy of <10 ppm (fig. S4).

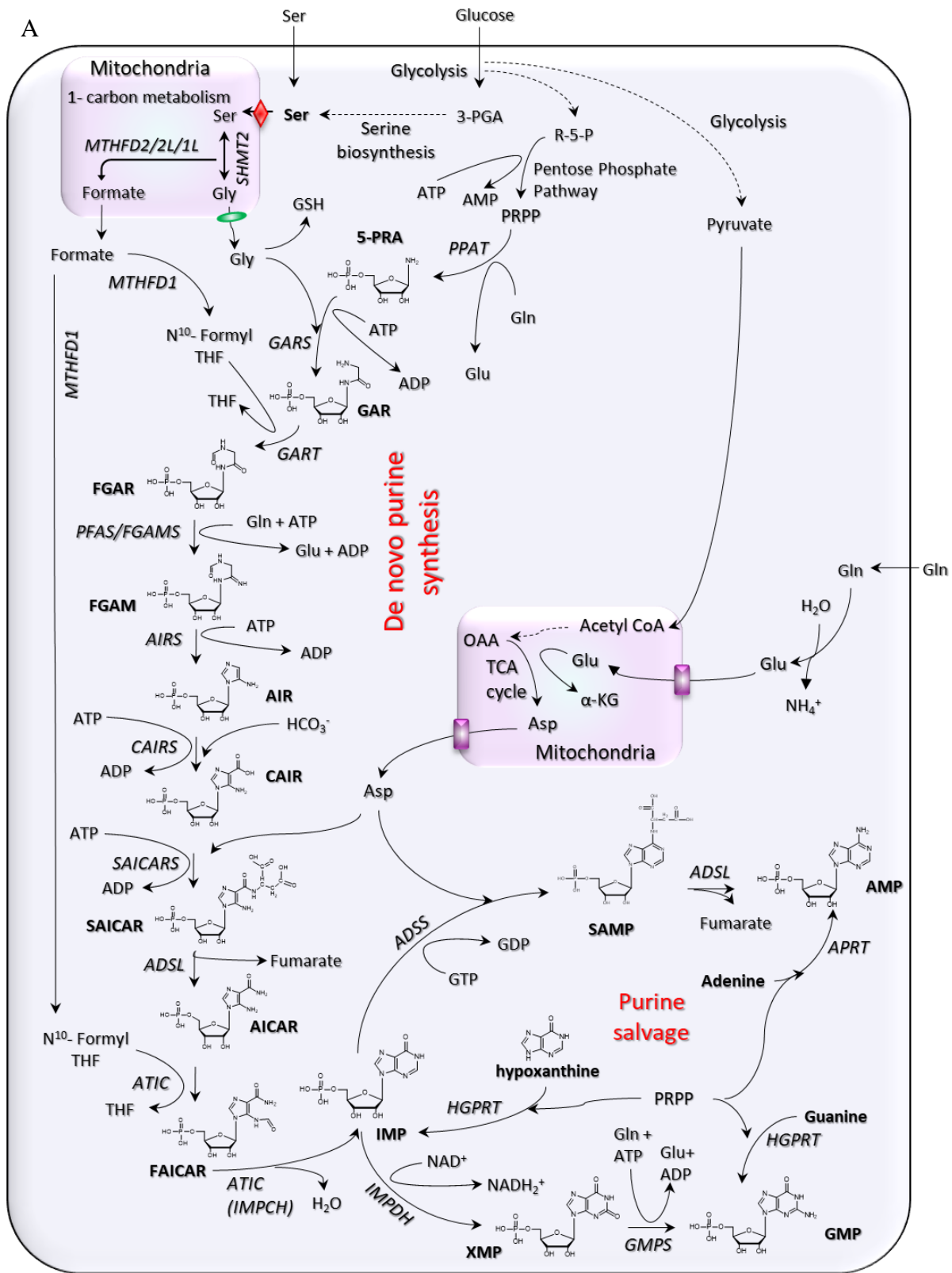
The chemical image and color overlay images were generated using Ionoptika Image Analyser (Version 2.0.2.11) (Ionoptika Ltd, UK). The unique molecular ions corresponding to <sup>15</sup>N AICAR/<sup>13</sup>C AICAR were selected with a mass window  $\Delta m/z = 0.01$  amu, centered at the accurate mass ( $m/z$  338.055) to obtain a map of its spatial distribution. The spread of ion counts/pixel for one representative sample is shown (fig. S7A inset. and fig. S7A). The color intensity at each pixel represents the relative signal intensity normalized to the maximum intensity of the selected ion in single pixel. Statistical analysis of pixels to obtain the information on its overall chemical composition has previously been described and validated in single bacterium to investigate the antibiotic accumulation (39).

Two criteria are used to filter out noise from the data *viz.*, 1) an intensity cutoff = 30% of the highest ion count/pixel or an ion count of 3, whichever was higher was applied; 2) Any outlier pixels that appeared out of the cell boundary are removed from the analysis. The analysis is performed for each sample layer independently. The spread of ion counts/pixel for the analyzed pixels after data pruning is shown (fig. S7B). The cumulative mass spectra of the AICAR pixels thus obtained, was compared with the cumulative spectrum from the pixels constituting cells in that layer (Fig. 4G). This allows one to investigate if purine de novo synthesis occurs in defined

$1 \times 1 \mu\text{m}^2$  pixels corresponding to the high concentration locus of the intermediate, AICAR. Upon  $^{15}\text{N}$  incorporation, the peak area for unlabeled and labeled AICAR at  $m/z$  337.06 and 338.05, AMP at  $m/z$  346.06 and 347.05, ATP ( $\text{Mg}^{2+}$  adduct) at  $m/z$  527.957 and 528.95 and GTP ( $\text{Mg}^{2+}$  adduct, - $\text{H}_2\text{O}$ ) at  $m/z$  525.94 and 526.87 ( $\Delta m/z = 0.02$  amu for all the selected ions) were determined. Then, the ratio of isotope labeled to the unlabeled ion of the selected metabolites (i.e., AICAR, AMP, GTP and ATP) were calculated for each layer independently (Fig. 4G inset and fig. S7E and G). Mean and standard deviation was determined by combining different layers of the sample (Fig. 4G and fig. S7D and F). Since isotopic enrichment in ATP was found to be significant in the labeled AICAR pixels, to rule out the possibility of interference from pyrimidine nucleotide signal at the peak assigned to ATP molecular ion, we determined the abundance of pyrimidine nucleotides from the HeLa P- cell LC/MS spectrum. The total abundance of pyrimidines was found to be much lower than ATP (fig. S7I).

**HeLa ATIC CRISPR- CAS9 knock out (ATIC K/O) cell culture and isotope incorporation:**

The ATIC K/O cells (30) were grown and maintained in RPMI (15% FBS) + 60  $\mu\text{M}$  adenine. For metabolite extraction and analysis with LC/MS or GCIB-SIMS imaging cells were grown on 100 mm culture dish or Si wafers, respectively. For isotope label incorporation studies, cells were transferred to purine depleted media RPMI (5% dFBS) for 12 hrs followed by 1x PBS wash and changing media to MEM (5%dFBS) and 60  $\mu\text{M}$   $^{15}\text{N}$  Ser or  $^{13}\text{C}$  Gly labeling for 4 hrs (bulk metabolite estimation with LC/MS) or 12 hrs (SIMS imaging). As expected, LC/MS analysis of cell extract from ATIC K/O cells did not show any  $^{15}\text{N}$  Ser mediated label incorporation into purine nucleotides, while it shows significant accumulation of AICAR (fig. S7H, and Fig. 4H, Supplementary Excel File4).



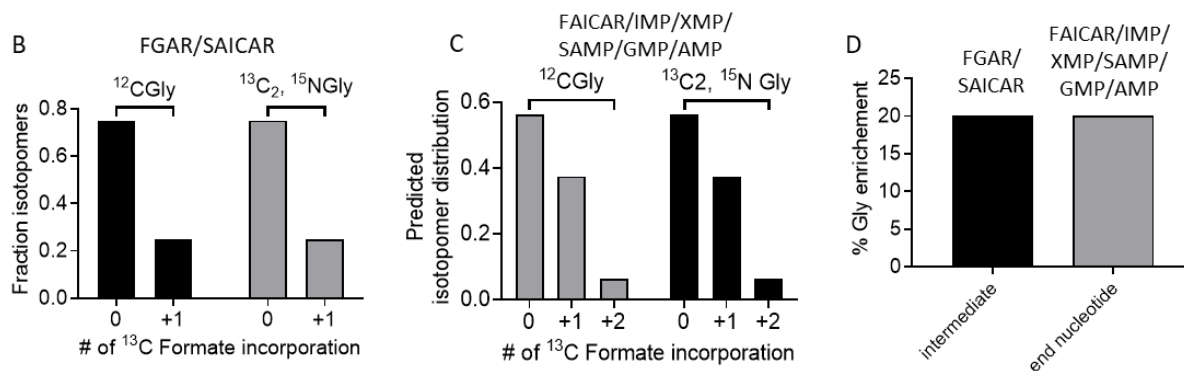


**Fig. S1 Purine synthesis and predictions of a diffusive model for DNPB.**

(A) De novo purine biosynthesis (DNPB) pathway involves ten consecutive steps starting with PRPP and building the nine-atom purine base ring to form IMP. Six different enzymes in higher organisms, including humans, catalyze these reactions. After IMP formation, the pathway is bifurcated to produce to GMP and AMP by the concerted action of the enzymes, IMPDH and GMPS, or ADSS and ADSL, respectively. Glycolytic pathway intermediates, glucose-6-phosphate and 3-PGA are used to produce, R-5-P and Ser, via the pentose phosphate pathway and the serine biosynthesis pathway, respectively. The glycolysis end product pyruvate is converted to acetyl coenzyme-A which feeds into the tricarboxylic acid cycle in the mitochondria. Mitochondrial metabolism is directly linked to the DNPB via the one carbon metabolism, tricarboxylic acid cycle and the electron transport chain that generate the building blocks and co-factor pool (Gly, Asp, formyl-THF and ATP) utilized in the DNPB pathway. Purine salvage involves the enzymes HGPRT and APRT that act on purine bases hypoxanthine (Hypo) or guanine and adenine, respectively, and PRPP to re-generate the purine mononucleotides (IMP, AMP and GMP). Acronyms: R-5-P: ribose-5-phosphate, Ser: serine, Ac CoA: acetyl coenzyme A, Asp: aspartic acid, Gly: glycine, Glu: glutamic acid,  $\alpha$ -KG: alpha- ketoglutarate, Gln: glutamine, OAA: oxaloacetic acid, 3-PGA: 3-phosphoglyceric acid, THF: tetrahydrofolate, NAD<sup>+</sup>: nicotinamide adeninedinucleotide-oxidized, NADH<sub>2</sub><sup>+</sup>: nicotinamide adeninedinucleotide-reduced, GSH: reduced glutathione, PRPP: phosphoribosyl pyrophosphate, 5-PRA: 5-phosphoribosylamine, GAR: glycinamide ribonucleotide, FGAR: phosphoribosyl-N-formylglycineamide, FGAM: formylglycinimidine ribonucleotide, AIR: 5-aminoimidazole ribonucleotide, CAIR: carboxyaminoimidazole ribonucleotide, SAICAR: phosphoribosyl aminoimidazole succinocarboxamide, AICAR: 5-aminoimidazole-4-carboxamide ribonucleotide, FAICAR: 5-formamidoimidazole-4-carboxamide ribonucleotide, IMP: inosine monophosphate, XMP: xanthosine monophosphate, SAMP: succinyladenosine monophosphate, AMP: adenosine 5'-monophosphate, GMP: guanosine-5'-monophosphate, ATP: adenosine triphosphate, GTP: guanosine triphosphate, ADP: adenosine diphosphate, GDP: guanosine diphosphate, *SHMT2*: serine hydroxymethyltransferase2 (mitochondrial isoform), *MTHFD2*: mitochondrial isoform, methylenetetrahydrofolate dehydrogenase/cyclohydrolase (mitochondrial isoform), *MTHFD1L/MTHFD2L*: methylenetetrahydrofolate dehydrogenase (NADP<sup>+</sup> dependent) 1/2 like, *MTHFD1*: methylenetetrahydrofolate dehydrogenase/cyclohydrolase (cytosolic isoform), *PPAT*: amidophosphoribosyl transferase, *GART*: trifunctional phosphoribosylglycinamide formyltransferase (GAR synthetase, GAR formyltransferase, and AIR synthetase), *PFAS/FGAMS*: phosphoribosylformylglycinimidine transferase, *PAICS*: bifunctional phosphoribosylaminoimidazole carboxylase and phosphoribosyl aminoimidazole succinocarboxamide synthase (CAIR synthetase, and SAICAR synthetase), *ADSL*: bifunctional

adenylosuccinate lyase, *ATIC*: bifunctional 5-aminoimidazole-4-carboxamide nucleotide formyltransferase/IMP cyclohydroxylase (IMPCH), *ADSS*: adenylosuccinate synthetase, *IMPDH*: IMP dehydrogenase, *GMPS*: GMP synthetase, *HGPRT*: hypoxanthine guanine phosphoribosyltransferase, *APRT*: adenine phosphoribosyltransferase. (♦) red diamond symbol: SFXN1, mitochondrial Ser transporter, (◊) green oval symbol: SLC25A38, mitochondrial Gly transporter, (◻) purple rectangle symbol: mitochondrial glutamate/aspartate transporter (SLC25A12/ SLC25A13). All enzymes are indicated in italics and metabolites in regular font. All purine intermediates and end product nucleotides are highlighted in bold. (B) The two isotopomers produced from unlabeled ( $^{12}\text{C}$  Gly: 0) and labeled GAR ( $^{13}\text{C}_2$ ,  $^{15}\text{N}$  Gly: +3) were treated as independent pools to calculate the  $^{13}\text{C}$  formate (1-y) fraction from the observed isotopomer abundance in FGAR and SAICAR, calculation described in methods section. (C) The isotopomer fractional distribution in SAICAR (Fig. 1F) and the calculated  $^{13}\text{C}$  formate enrichment (1-y) was used to predict the isotopomer distribution in FAICAR and all the downstream purine nucleotides. (D) Following the model,  $^{13}\text{C}_2$ ,  $^{15}\text{N}$  Gly (1-x) enrichment in the observed intermediates and the simulated values in the newly synthesized end nucleotides will be same. The calculations performed on one representative dataset are shown as an example.

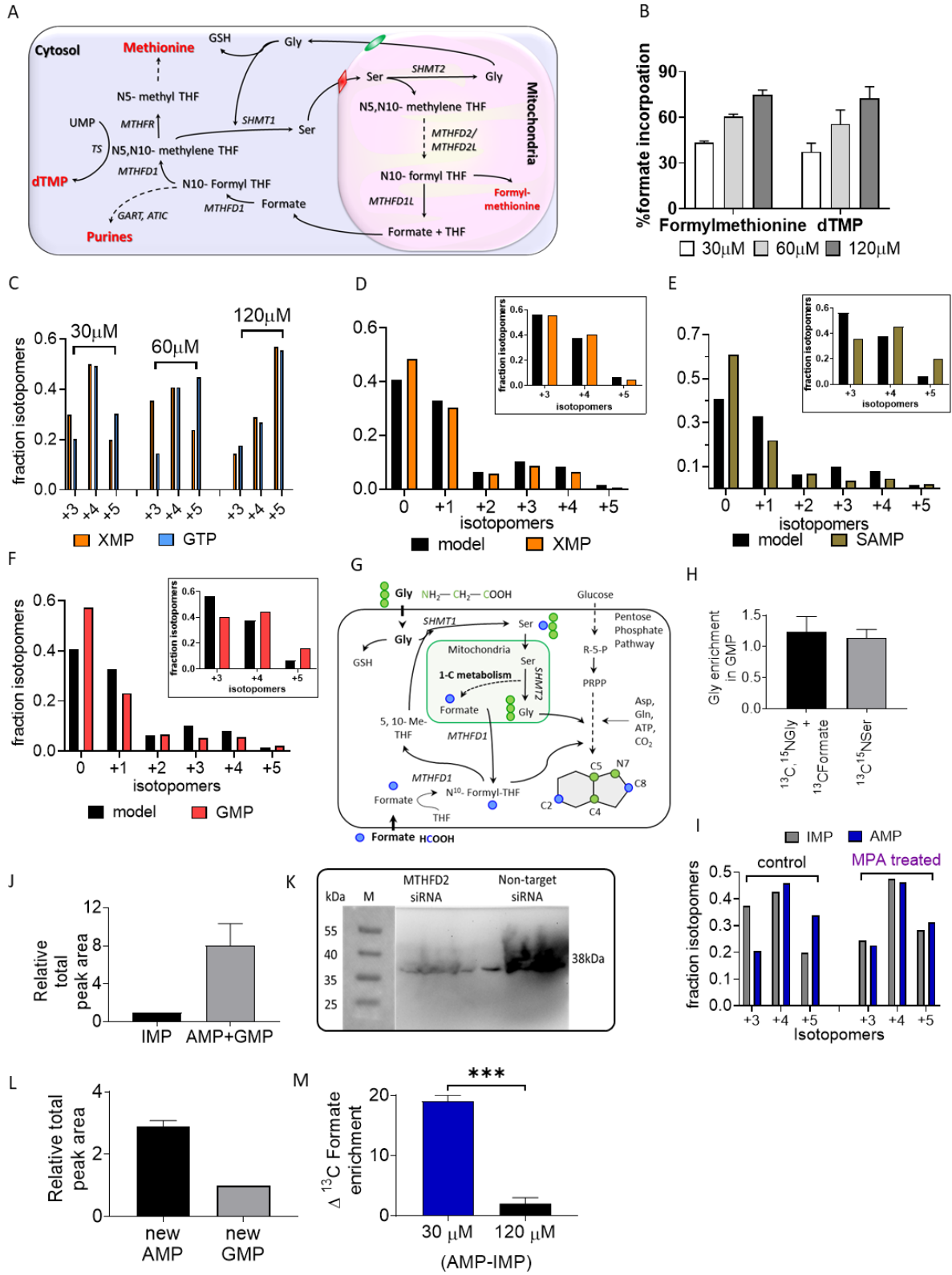
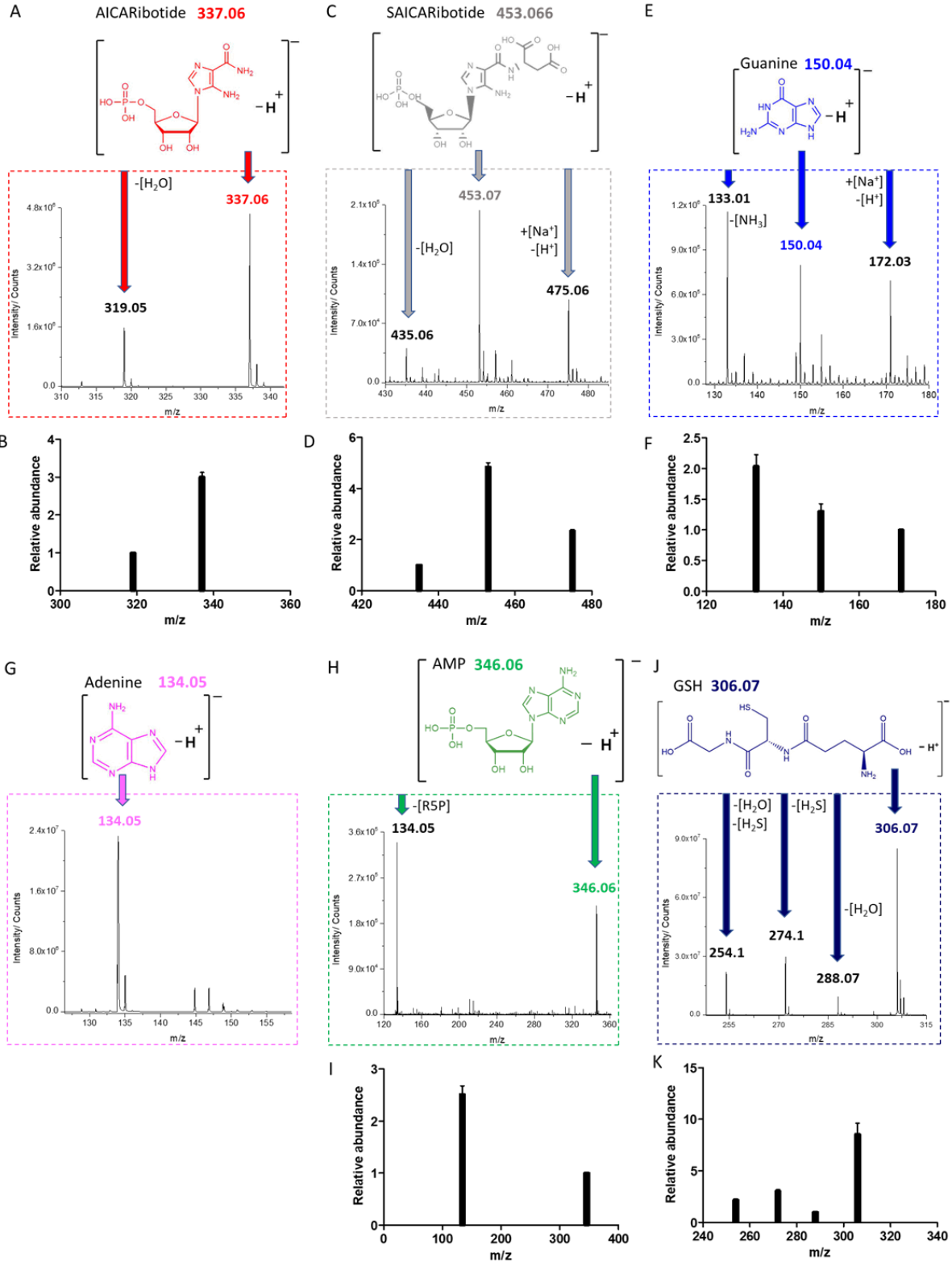


**Fig. S2 Leveraging mitochondrial metabolism to probe metabolic channeling in DNPB pathway.**

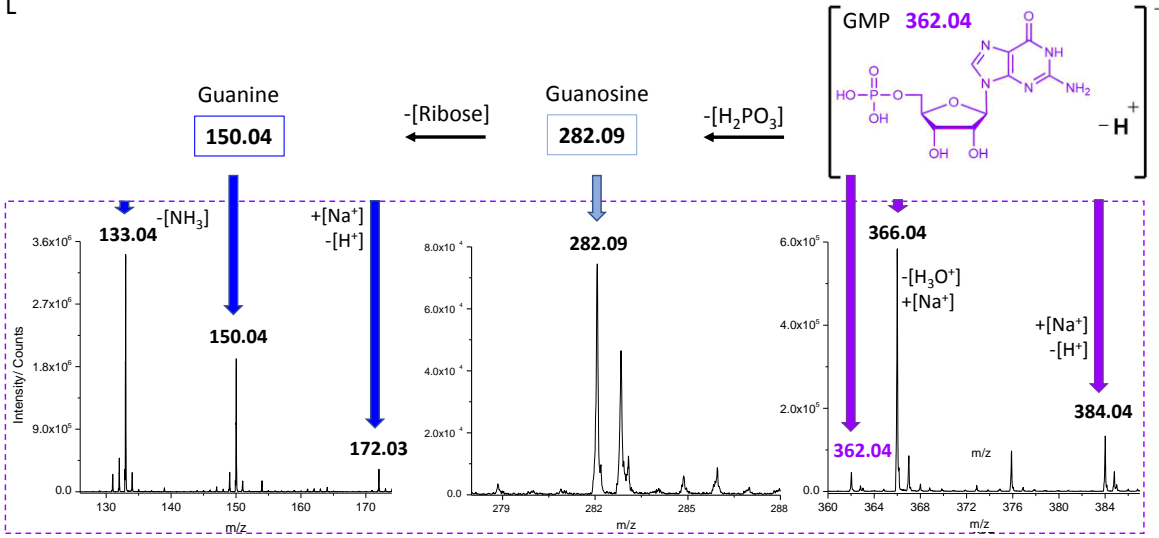
(A) Schematic for one carbon metabolism and the involvement of mitochondrial enzymes. Due to the compartmentalized generation of formylmethionine, the level of isotope incorporation in it reports the state of mitochondrial 10-formyl-THF levels. Ser is transported into mitochondria using the mitochondrial Ser transporter, SFXN1. Inside mitochondria, Ser is metabolized by the enzyme *SHMT2*, generating 5,10-methylene-THF and Gly. 5,10-methylene THF is further transformed by the enzymes *MTHFD2/MTHFD2L* to produce 10-formyl-THF (used for mitochondrial formylmethionine production) and finally *MTHFD1L* action releases formate and THF. The Gly and formate thus produced in mitochondria is released back into the cytoplasm. The cytoplasmic enzyme *MTHFD1* converts formate and THF to 10-formyl-THF (used in purine de novo biosynthesis) and further to 5,10-methylene THF (used in deoxythymidine monophosphate, dTMP, production by the enzyme thymidylate synthase (*TS*)). The reduced form of the cofactor 5-methyl THF, produced by the enzyme methylene tetrahydrofolate reductase (*MTHFR*), is utilized in methionine synthesis. Glycine is used for GSH synthesis. (B) For the in vivo isotope tracer experiments, as the isotopically labeled Ser concentration was varied from 30- 120  $\mu\text{M}$ ,  $^{13}\text{C}$  formate production increased, reflected in the percentage isotope enrichment in formylmethionine and dTMP. (C) The isotopomer distribution in GMP was compared to its precursor, XMP, after labeling with 30- 120  $\mu\text{M}$   $^{13}\text{C}_3$ ,  $^{15}\text{N}$  Ser, for 4 hrs. While at low concentration (30  $\mu\text{M}$ ), the two nucleotides show different isotopomer distribution of their newly synthesized species (+3, +4 and +5), at 120  $\mu\text{M}$   $^{13}\text{C}_3$ ,  $^{15}\text{N}$  Ser, this difference is not retained. Thus, for all the bulk metabolic measurements 30  $\mu\text{M}$   $^{13}\text{C}_3$ ,  $^{15}\text{N}$  Ser or 30  $\mu\text{M}$   $^{13}\text{C}_2$ ,  $^{15}\text{N}$  Gly and formate were used, unless specified. Values from one representative experiment are shown. (D) When 30  $\mu\text{M}$   $^{13}\text{C}_3$ ,  $^{15}\text{N}$  Ser was used for labeling, the isotopomer distribution observed in XMP matched with the simulated values obtained from the model, while (E) isotopomer distribution in the newly synthesized SAMP and (F) newly synthesized GMP were different. This shows that, FGAR, SAICAR, IMP and XMP are derived from the same pool of intermediates, whereas SAMP and the end product nucleotides, AMP and GMP, are derived from a different pool of intermediates that does not equilibrate with the bulk of cytosol. The insets in (D), (E), and (F) show the overlay of the observed fractions of +3, +4 and +5 isotopomers for XMP, SAMP and GMP, respectively, with the simulated values from the model. (G) Schematic to explain the flow of isotopically labeled  $^{13}\text{C}_2$ ,  $^{15}\text{N}$  Gly and  $^{13}\text{C}$  formate supplied in molar equivalents in the growth media. Labeled Gly combines with 5,10-methylene THF (Me-THF) by the action of the enzyme SHMT2 and regenerates  $^{13}\text{C}_3$ ,  $^{15}\text{N}$  Ser. Labeled Ser thus produced is used in the mitochondrial one carbon metabolism leading to the production of labeled Gly and formate within mitochondria. (H) When the two labeled substrates,  $^{13}\text{C}_2$ ,  $^{15}\text{N}$  Gly and  $^{13}\text{C}$  formate were provided in the media, action of the enzymes MTHFD1 and SHMT1 regenerates labeled Ser in cytosol, as indicated by the appearance of a +4 labeled species of Ser ( $^{13}\text{C}_3$ ,  $^{15}\text{N}$ ), data not shown, which can now enter the mitochondria and be metabolized further. Thus, under these conditions, we still observed channeled AMP/GMP generation. The Gly incorporation under Gly+Formate was normalized by the respective incorporation in GSH and dTMP to normalize for the difference in the rate of uptake of the substrates. and Percentage Gly incorporation in GMP when isotopically labeled  $^{13}\text{C}_2$ ,  $^{15}\text{N}$  Gly and  $^{13}\text{C}$  formate were supplied in the media compared with that under  $^{13}\text{C}_3$ ,  $^{15}\text{N}$  Ser supplementation. All values were normalized by the %  $^{13}\text{C}_2$ ,  $^{15}\text{N}$  Gly incorporation in reduced glutathione to limit the variability in experimental replicates and differences in the cellular uptake of Ser and Gly. Similar normalization has also been applied to the AMP enrichment data shown in (Fig. 2H). (I) Mycophenolic acid treatment



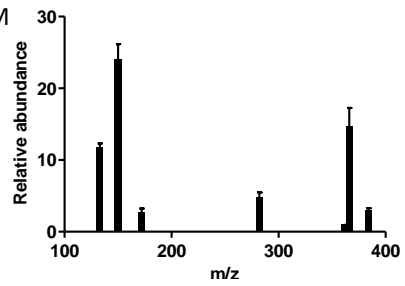
for 1hr affected the isotopomer distribution in IMP such that the IMP accumulated after MPA treatment showed the same isotopomer distribution as that in AMP produced. **(J)** The output of the three mononucleotides IMP (flux via the diffusive pathway) and AMP+GMP (flux of “channeled” pathway) were compared for each  $^{13}\text{C}_3$ ,  $^{15}\text{N}$  Ser labeling experiment. The newly synthesized AMP and GMP amounts were calculated as described in Methods section. **(K)** Western blot analysis shows a clear decrease in the abundance of the mitochondrial enzyme MTHFD2 52 hrs post transfection with MTHFD2 siRNA compared to the non-target siRNA. **(L)** Division of IMP into guanine and adenine nucleotides was probed using  $^{13}\text{C}_3$ ,  $^{15}\text{N}$  Ser incorporation as the reporter of de novo synthesis. Synthesis via de novo pathway showed preferential partitioning of IMP towards AMP compared to GMP. **(M)** Compared to a low concentration of 30  $\mu\text{M}$ , when 120  $\mu\text{M}$  of labeled Ser was used for labeling, the difference in % formate incorporation between IMP and AMP drops from ~18% to <5%. This indicates homogeneous  $^{13}\text{C}$  formate availability in the cytosolic bulk arising as a result of high labeled formate production. Three or four biological replicates and 1 or 2 technical replicates were performed for each experiment. Isotope incorporation values represent mean of three or four experiments with SD as the error bars **(B)**, **(H)**, **(J)**, **(L)**, **(M)** or values from one representative experiment is shown **(C)**, **(D)**, **(E)**, **(F)**, **(I)**.



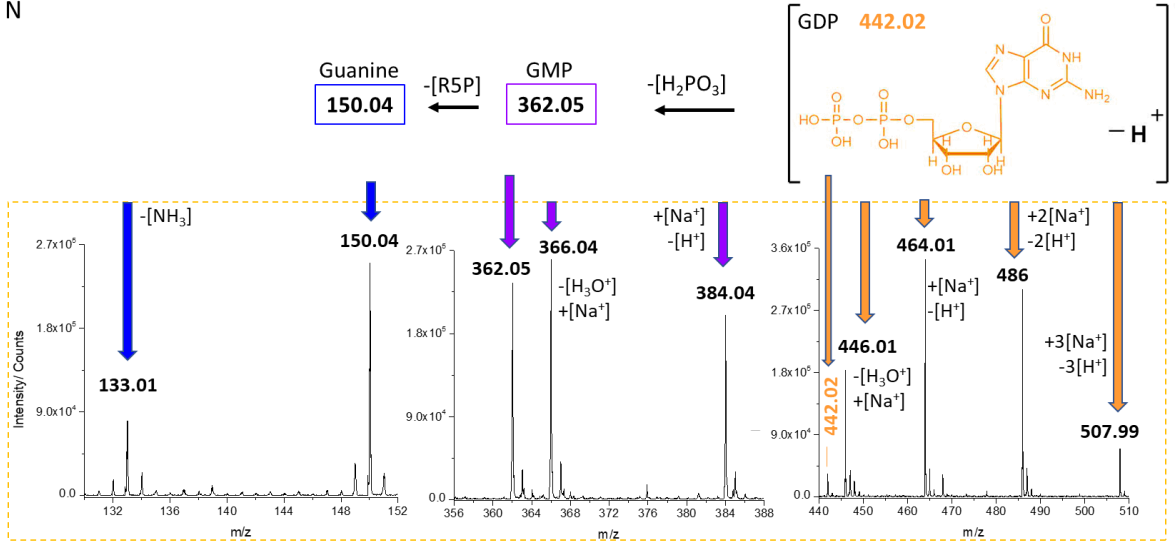
L



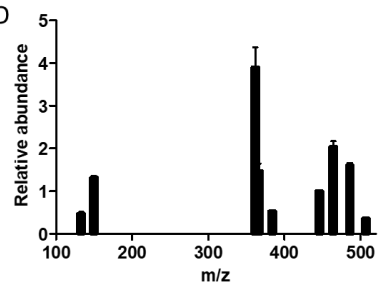
M



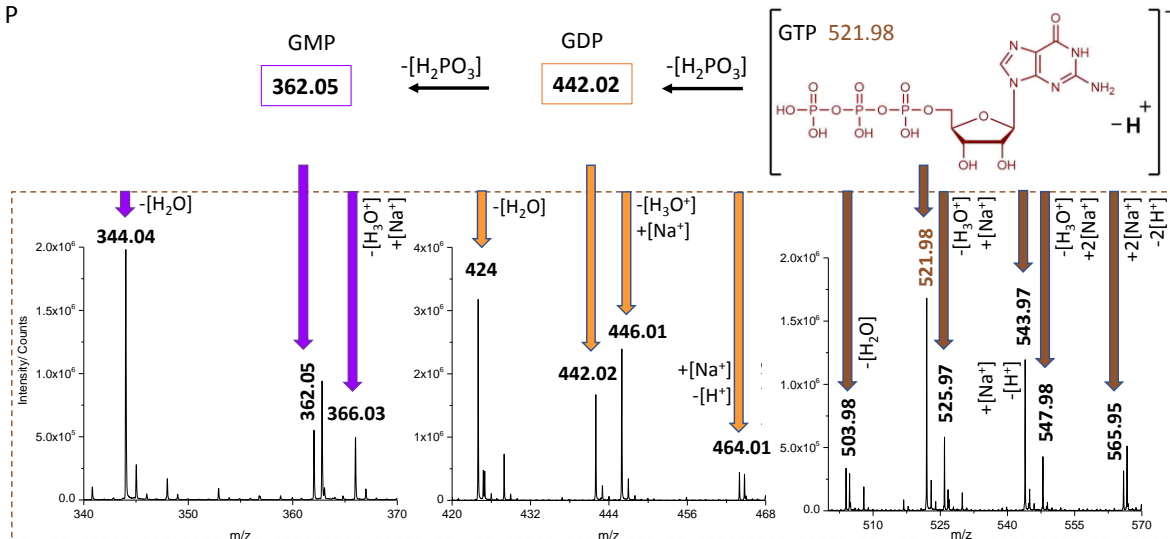
N



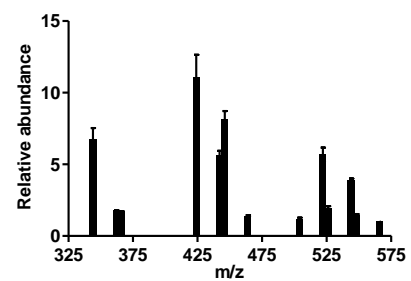
O



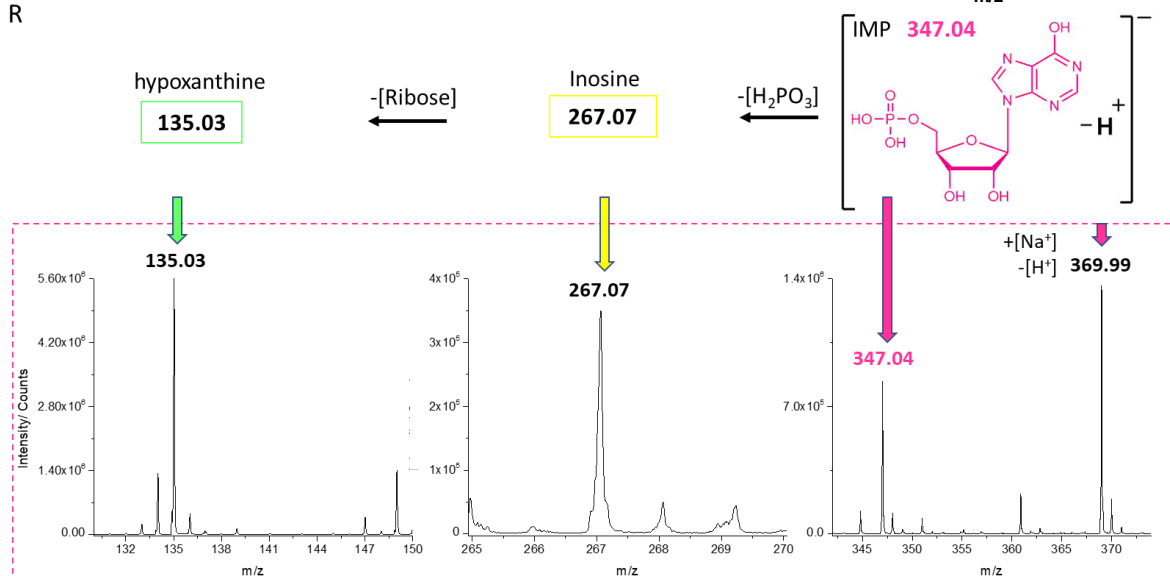
P



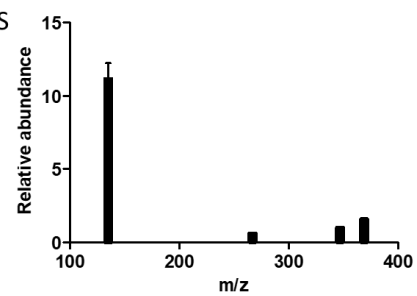
Q



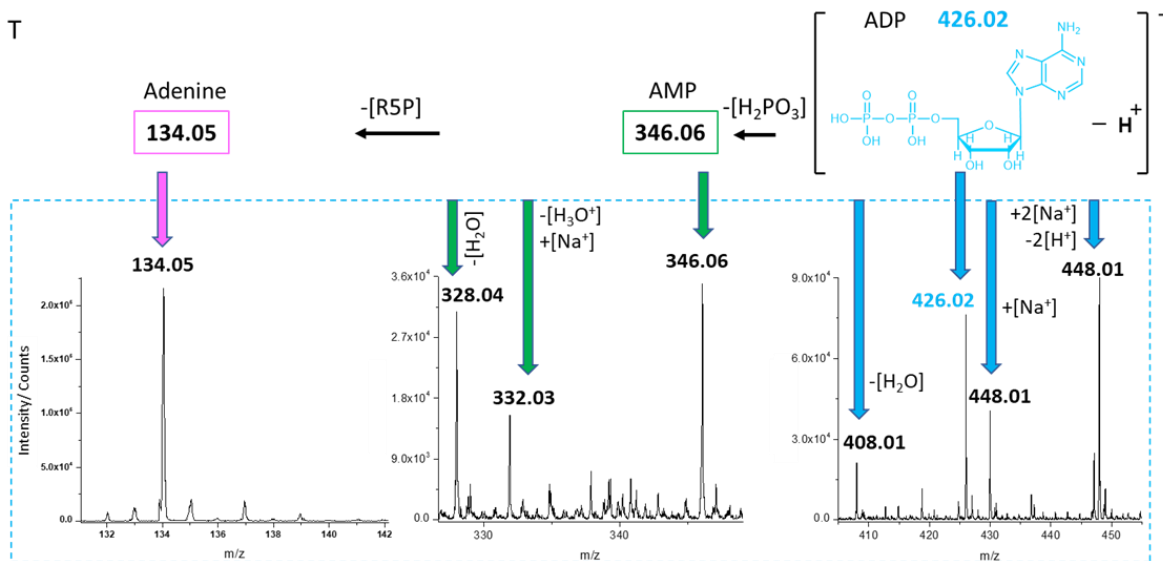
R



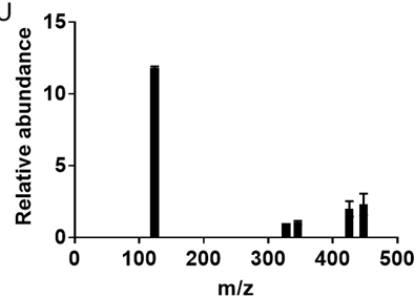
S



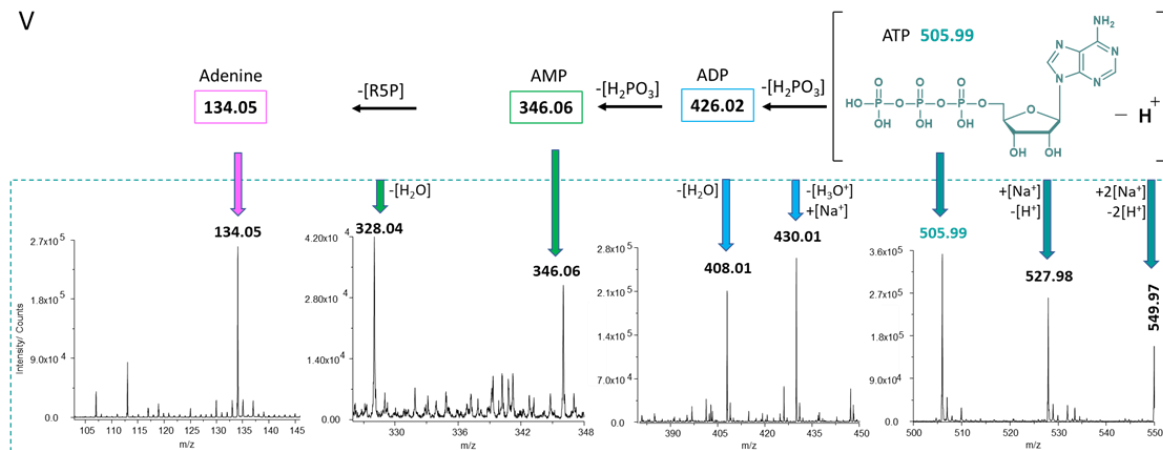
T



U



V



W

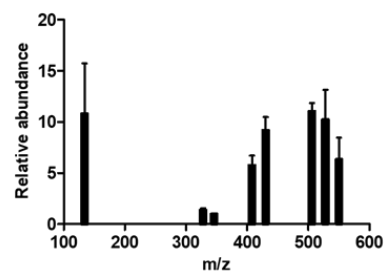


**Fig. S3 Structure and the observed intact molecular ions and adduct and fragment ions of select metabolite standards under GCIB-SIMS.**

Purines and reduced glutathione spectra were collected under GCIB-SIMS (70KeV), negative ion mode. (A), (C), (E), (G), (H), (J), (L), (N), (P), (R), (T), (V) molecular structures of AICARibotide, SAICRibotide, Guanine, Adenine, AMP, reduced glutathione (GSH), GMP, GDP, GTP, IMP, ADP and ATP, respectively, with the isotope peak assignments for the respective pseudomolecular ions, salt adducts and fragment ions. (B), (D), (F), (I), (K), (M), (O), (Q), (S), (U), (W) the relative intensities of all the major ionic species observed for AICARibotide, SAICRibotide, Guanine, AMP, reduced glutathione (GSH), GMP, GDP, GTP, IMP, ADP and ATP. The area under the curve over 1024 pixels, using 0.02  $\Delta m/z$  window, at the center of the peak of interest was used for plotting their relative abundances. The fragment ions generated after loss of purine ring (i.e., composed of the phosphate backbone or the pentose sugar) are not included in this analysis, since the in-vivo experiments involved labeling only of the purine base atoms.

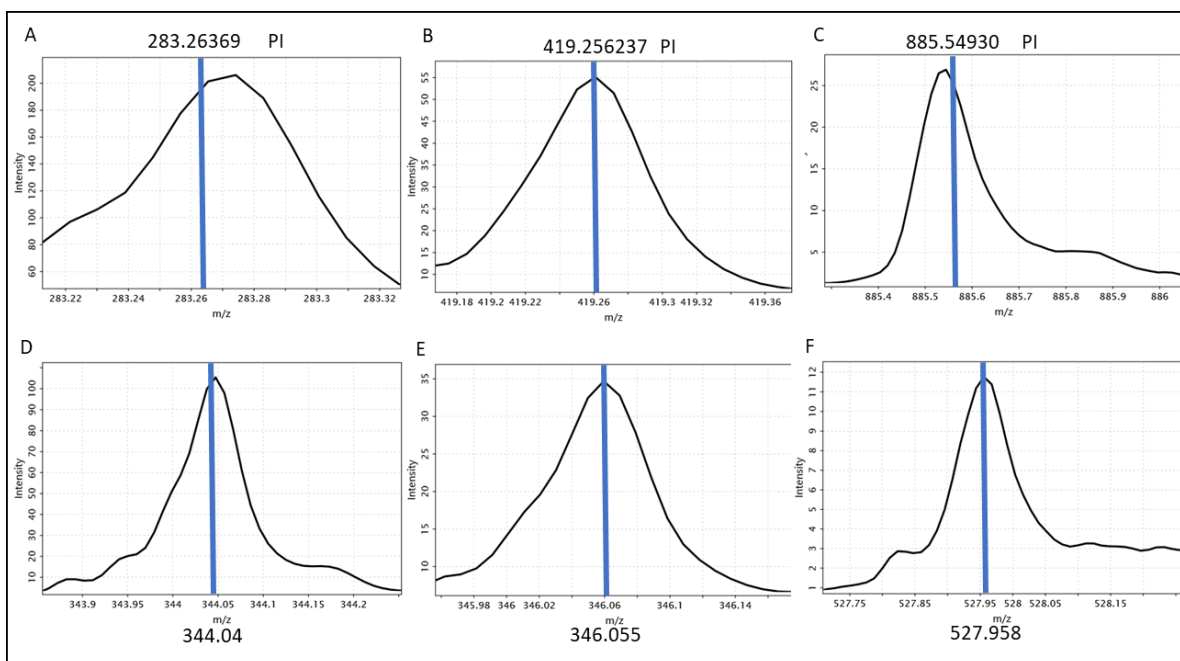


**Fig. S4 Post-acquisition calibration for GCIB-SIMS imaging.** (A), (B), (C) Three fragment ion species (fragment from inositol di and triphosphate,  $\text{PIP}_3$  and  $\text{PIP}_2$ -  $m/z$  283.26369 and 419.25623, and PI lipid, 38:4-  $m/z$  885.54930) corresponding to low, middle and high mass range, respectively, generated from PI lipid were used for post-acquisition calibration of all the ToF-SIMS spectrum of HeLa cells samples. Several peaks corresponding to known metabolites of interest were inspected after calibration. Some examples, with their respective calculated  $m/z$  values, are shown in (D) pseudo-molecular ion of cGMP/GSH (sodium adduct), (E) pseudo-molecular ion AMP (dehydrated), and (F) ATP molecular ion (dimagnesium adduct), respectively. All the peaks were found to be correctly centered at their respective calculated  $m/z$  values.

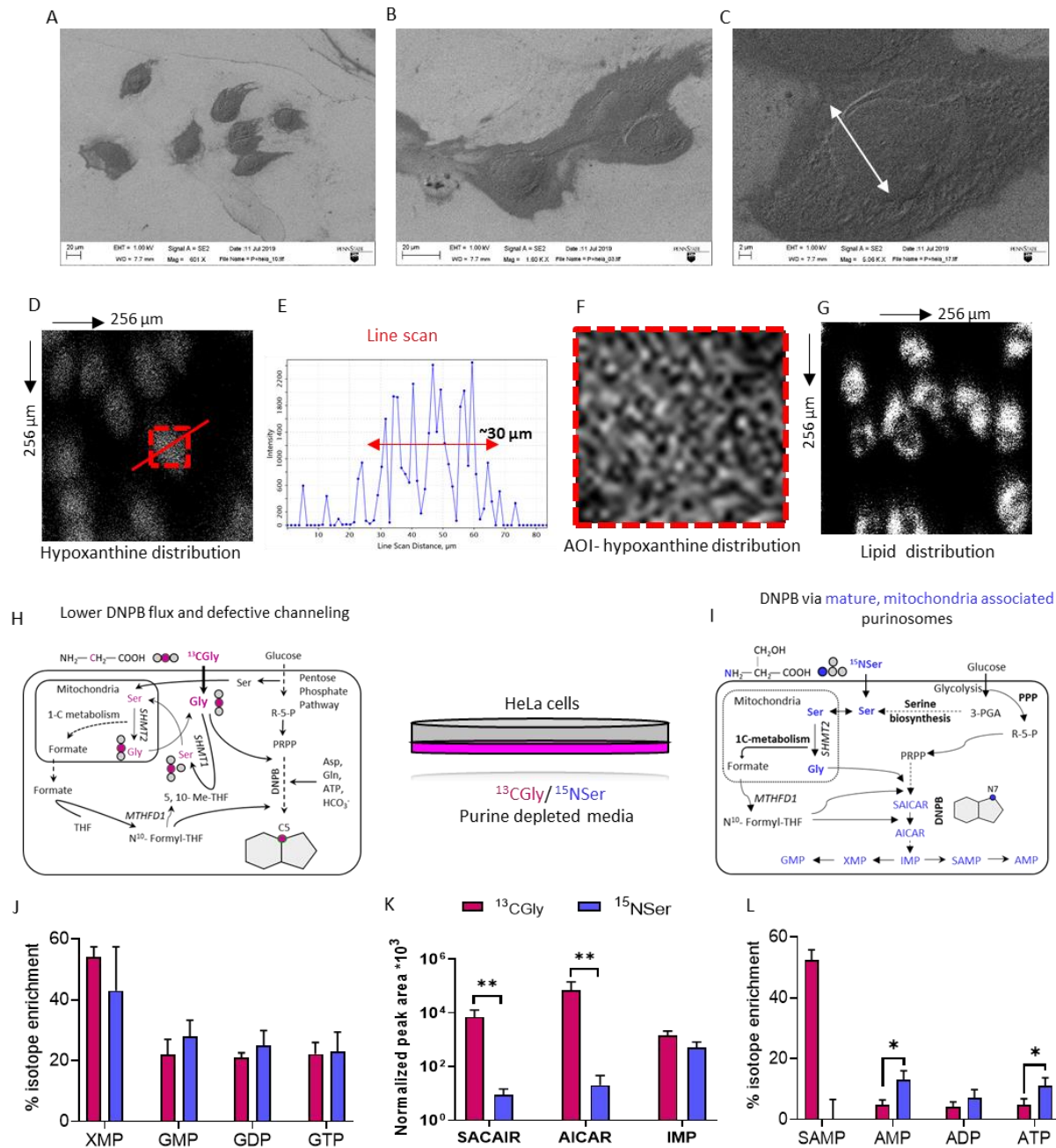


**Fig. S5 Probing the frozen hydrated cell morphology and validating the use of singly labeled  $^{15}\text{Nser}$ .** (A), (B), and (C) the representative cryo-SEM images of P+ HeLa cells. Several P- and P+ HeLa cells were examined at multiple magnifications to ascertain that the overall cell morphology remained close to the hydrated native state. The cell nucleus is marked in white arrow and measures  $\sim 15.5 \mu\text{m}$ . (D) Hypoxanthine distribution in layer-3 of a representative P- HeLa cell sample. Image was generated using  $135.03 m/z$  and shows a homogenous distribution throughout the cellular volume. (E) Line scan (dashed line in (D)) gives an estimate of lateral cell dimensions in each analyzed layer (Intensity corresponds to a single voxel intensity across the line scan). (F) Zoomed-in view of the area of interest (shown in red dashed line (D)). The cellular boundary was determined by combining the spatial distribution of Hypo and (G) PI lipid fragment (10% signal intensity baseline was used for each ion). The lipid distribution clearly shows a low intensity region



in the center, corresponding to nuclear volume. **(H)**, and **(I)** show the isotope label flow into the purine base ring when cells are grown with  $^{13}\text{C}$  Gly or  $^{15}\text{N}$  Ser, respectively. The possibility of using singly labeled  $^{15}\text{N}$  Ser to capture active purinosomes was explored, since the use of multiply labeled  $^{13}\text{C}_3$ ,  $^{15}\text{N}$  Ser was not practical for SIMS analysis (owing to the division of purine intermediates and end nucleotides into multiple isotopomers, thus making it difficult to obtain significant signal from a  $1\ \mu\text{m} \times 1\ \mu\text{m} \times 350\text{-}400\ \text{nm}$  of cellular volume). **(H)** When Gly is supplied in excess, it is known to generate Ser by the enzyme SHMT1, by utilizing the available 5,6-methylene THF. This causes a disbalance in the availability of 10-formyl THF, essential for conversion of AICAR to IMP by the enzyme ATIC (*17*). We hypothesized that this would cause lower DNPB flux, accumulation of AICAR and plausible leakage of the intermediates from the channeled pathway. **(J)** As expected, under excess  $^{13}\text{C}$  Gly ( $60\ \mu\text{M}$ , 4 hrs) supply, significant AICAR accumulation was observed compared to  $^{15}\text{N}$  Ser ( $60\ \mu\text{M}$ , 4hrs) supply. Comparison of label incorporation in guanine (**K**) and adenine (**L**) nucleotides when  $^{13}\text{C}$  Gly or  $^{15}\text{N}$  Ser were used for label incorporation. Adenine nucleotides AMP and ATP showed a significantly higher isotope incorporation upon  $^{15}\text{N}$  Ser labeling, compared with  $^{13}\text{C}$  Gly labeling. The same was not found to be true for guanine nucleotides, likely because when generated in an unchanneled manner, IMP is preferentially branched to guanine nucleotides (fig. S2K). Our analysis established the utility of singly labeled  $^{15}\text{N}$  Ser to monitor channeled DNPB pathway by SIMS and use  $^{13}\text{C}$  Gly as a negative control.

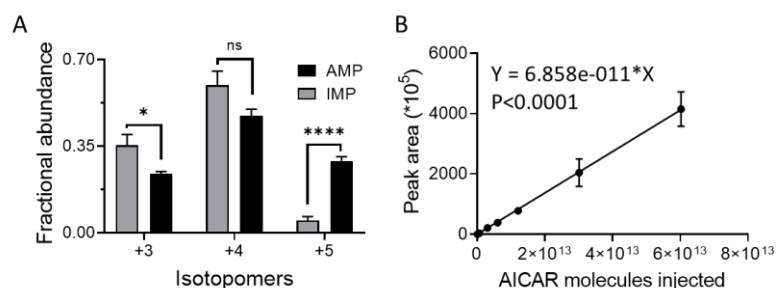


**Fig. S6 Metabolite estimations in HeLa cells labeled for 14 hours.** (A) Mean and SD for the +3, +4, and +5 isotopomer fractional abundance distribution was obtained from three independent  $^{13}\text{C}_3$ ,  $^{15}\text{N}$  Ser incorporation experiments. The respective abundance of +3, +4 and +5 for AMP and IMP were compared and independent t-tests were performed on the ratio of each isotopomer abundance for the two metabolites. \*\*\*\*, \*, and ns correspond to the P value of  $<0.00005$ ,  $<0.05$ , and  $>0.05$ , respectively. (B) Standard curve for AICAR known concentrations was plotted using the observed peak area for each analyzed concentration. The values were used to perform linear regression analysis forcing y intercept at zero. The equation for the fit and the corresponding *P* value are provided.

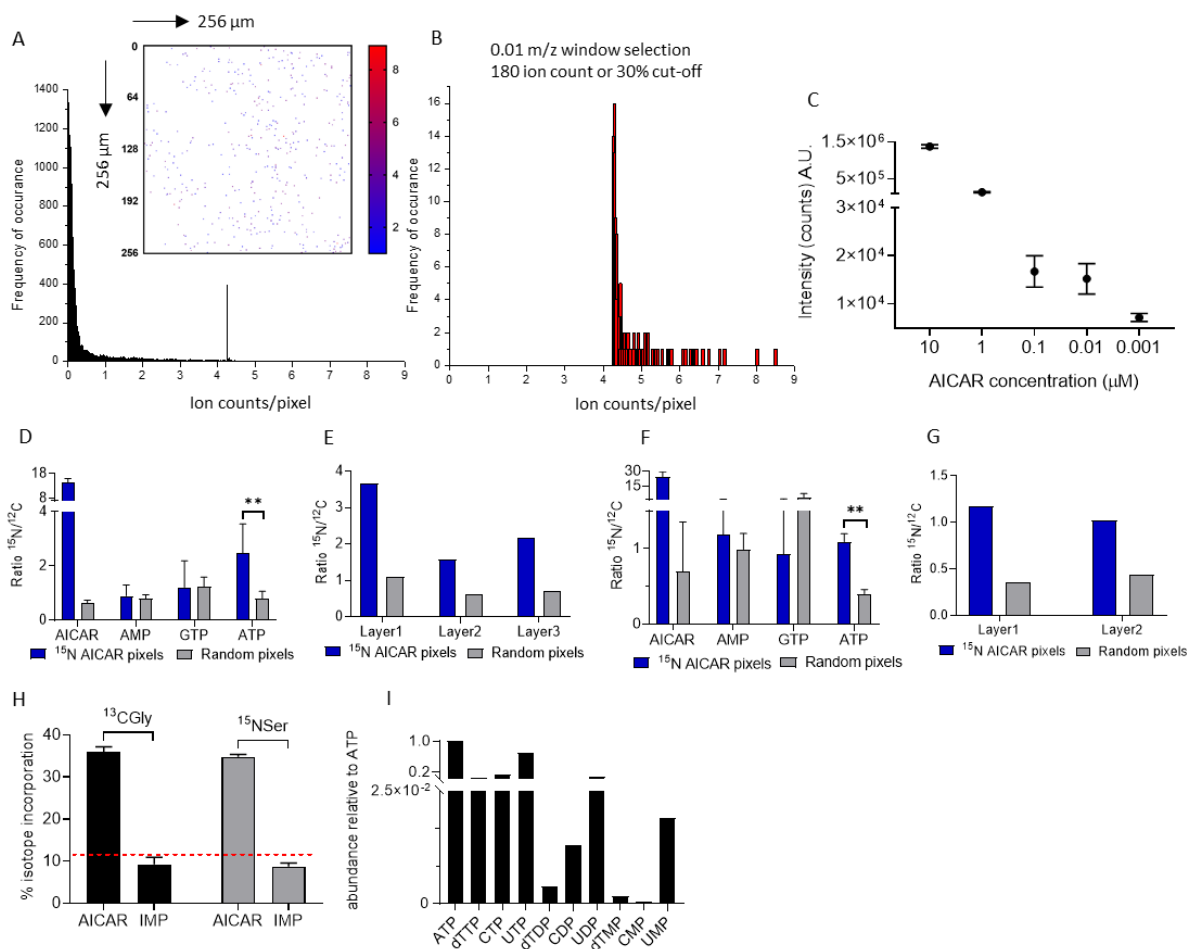


**Fig. S7 Labeled AICAR pixel analysis to probe channeling in single cells.** (A) The plot shows the frequency distribution of ion counts/pixel (Ion counts per pixel= Intensity per pixel/ 60) for all the pixels obtained by 0.01  $\Delta m/z$  mass selection at  $m/z$ - 338.053 (corresponding to  $^{15}\text{N}$  labeled AICAR), for layer 3 of one representative frozen hydrated HeLa cell samples. Inset: Ion current corresponding to the selected  $m/z$  value across the whole field view. Pixel color represents the ion current variation, reporting back on the abundance of the selected ion. (B) Shows the ion count/pixel after applying the following criteria: 1) 30% of maximum intensity/pixel observed for the selected mass peak or 180 intensity/pixel (corresponding to  $\sim 3$  ion/pixel), whichever was higher, to select the  $^{15}\text{N}$  AICAR pixels for further analysis. 2) While 98% of the filtered pixels resided within cell boundary, any pixels outside the cells were rejected from the analysis. Lateral distribution of these pixels is shown in (Fig. 4E). (C) Under the same SIMS conditions used for the cell analysis, the concentration dependence of the SIMS signal intensity for AICAR was studied. SIMS spectra was generated and the cumulative pixel intensity across a  $32 \times 32 \mu\text{m}^2$  total field view was plotted for each concentration. Mean and SD of two independent measurements, with 6 technical replicates each is plotted. (D) and (F) Biological replicates of the results described in (Fig. 4G). Level of  $^{15}\text{N}$  enrichment in the purine de novo synthesis intermediate, AICAR and the end product nucleotides, AMP, GTP and ATP was compared for the  $^{15}\text{N}$  AICAR pixels and equivalent number of random pixels selected from across the cell. Error bar corresponds to the variation observed for each layer analyzed for a sample. The ratio of total signal intensity for the unique peak corresponding to the isotope enriched ( $^{15}\text{N}$  labeled) and the respective unlabeled ( $^{12}\text{C}$ )

molecule of interest was determined for each layer using  $\Delta m/z = 0.02$ , centered at the expected exact mass corresponding to the molecular ions of interest. **(E)** and **(G)** In each layer analyzed, the ratio of  $^{15}\text{N}$  ATP/  $^{12}\text{C}$  ATP in the AICAR pixels was consistently found to be higher than that in the random pixels selected from whole cell. **(H)** ATIC CRISPR-CAS9 HeLa cells were incubated with 60  $\mu\text{M}$   $^{15}\text{N}$  Ser or  $^{13}\text{C}$  Gly for 4h and label incorporation was determined by LC/MS. While AICAR showed ~25% label incorporation in AICAR, the product of ATIC reaction, IMP, showed no isotope enrichment. Red dotted line shows the +1 isotopic peak abundance as expected from natural abundance of  $^{15}\text{N}$  and  $^{13}\text{C}$ . **(I)** To rule out the possibility of signal interference from pyrimidine nucleotides towards the SIMS peak assigned for the molecular ion from ATP ( $[\text{ATP-H}_3+\text{Mg}^{2+}]^{-1}$  -  $m/z$ - 527.96), the total abundance of pyrimidine nucleotides relative to ATP was estimated from LC/MS analysis of P- HeLa cell extracts. Estimates from one representative experiment are shown.

**Table S1 Reagents used in the study with the respective catalogue numbers and source.**

S. No.	Reagent name	Catalogue number	Company
1	$^{13}\text{C}_2, ^{15}\text{N}$ Gly	CNLM-1673	Cambridge Isotope Laboratory, USA
2	$^{13}\text{C}_3, ^{15}\text{N}$ Ser	CNLM-474	Cambridge Isotope Laboratory, USA
3	$^{15}\text{N}_4$ hypoxanthine	NLM-8500	Cambridge Isotope Laboratory, USA
4	$^{13}\text{C}$ Sodium Formate	279412	Sigma Aldrich, USA
5	$^{15}\text{N}$ Ser	609005	Sigma Aldrich, USA
6	$^{13}\text{C}$ Gly	279439	Sigma Aldrich, USA
7	Adenine	10496	Sigma Aldrich, USA
8	Hypoxanthine	3200	PL Biochemicals, USA
9	Guanine	G0381	Sigma Aldrich, USA
10	ATP sodium salt	A3377	Sigma Aldrich, USA
11	GTP sodium salt	G8877	Sigma Aldrich, USA
12	Glutathione (reduced)	G4251	Sigma Aldrich, USA
14	ADP sodium salt	1171	CalBiochem, USA
15	GDP sodium salt	G7127	Sigma Aldrich, USA
16	AMP	A1752	Sigma Aldrich, USA
17	GMP disodium salt	G8377	Sigma Aldrich, USA
18	5-aminoimidazole-4-carboxamide-1- $\beta$ -D-furanosyl monophosphate (AICARibotide)	311705	Toronto Research Chemicals INC, Canada
19	N-succinyl-5-aminoimidazole-4-carboxamide ribose-5'-phosphate (SAICARibotide)	S688795	Toronto Research Chemicals INC, Canada
20	Trehalose	T9531	Sigma Aldrich, USA
21	Serine	S260	Sigma Aldrich, USA
22	Glycine	G7126	Sigma Aldrich, USA
23	Inosine monophosphoric acid (IMP)	I4625	Sigma Aldrich, USA

**Table S2 Metabolites with their observed retention time (min), the calculated  $m/z$  for the molecular ion  $[M-H]^{-1}$ , and the molecular formula of the ion.** The  $m/z$  values of the molecular ions are used to calculate the  $m/z$  for different fragment and adduct ions and the expected  $m/z$  after different isotope label incorporations. The values are used for LC/MS and GCIB-SIMS spectra analysis and peak assignment (fig. S3).

Metabolite	Elution time (min)	Calculated $m/z$ $[M-H]^{-}$	Molecular formula
Adenine	4.3	134.0472	C5H4N5
Guanine	3.08	150.0421	C5H4N5O
ATP	15.12	505.9885	C10H15N5O13P3
ADP	13.9	426.0221	C10H14N5O10P2
AMP	11.63	346.0558	C10H13N5O7P
GTP	15.0	521.9834	C10H15N5O14P3
GDP	13.6	442.0170	C10H14N5O11P2
GMP	10.5	362.0507	C10H14N5O8P
Hypoxanthine	2.5	135.0312	C5H3N4O
PRPP	14.8	388.9445	C5H12O14P3
IMP	10.35	347.0398	C10H12N4O8P
ITP	14.9	506.9725	C10H14N4O14P3
GAR	1.7	285.0493	C7H15N2O8P
SAICAR	14.45	453.0664	C13H18N4O12P
AICAR	10.3	337.0555	C9H14N4O8P
XMP	13.3	363.0347	C10H12N4O9P
SAMP	14.5	462.066	C14H17N5O11P
Chlorpropamide	16.8	275.0267	C10H12ClN2O3S
dTMP	11.4	321.0493	C10H15N2O5P
Formylmethionine	12.5	176.0386	C6H10NO3S
Glutathione (reduced)	8	306.076	C10H17N3O6S

FGAR	6.8	313.045	C8H15N2O9P
FAICAR	5.8	365.0498	C10H15N4O9P
dGTP		505.993	C10H15N5O13P3

---

**Table S3** The atomic mass unit difference ( $\Delta amu$ ) upon incorporation of the respective isotope labeled atoms or molecule. Masses are used to compute the exact molecular weight of the labeled intermediates and end products of DNPB pathway.

Molecule/atom	$\Delta amu$
$^{13}C_2, ^{15}NGly$	3.0037
$^{13}C$	1.0033
$^{15}N$	0.997
$Mg^{2+}$	23.985

**Data S1.** Description of the diffusive model described in Fig 1

**Data S2.** Data for Fig. 2A- C and fig. S2B- F and M

**Data S3.** Data for Fig. 2D-F and K

**Data S4.** Data for fig. S5J to L, S6A, and S7H .



## References

1. E. Villa, E. S. Ali, U. Sahu, I. Ben-Sahra, Cancer Cells Tune the Signaling Pathways to Empower de Novo Synthesis of Nucleotides. *Cancers* **11**, 688 (2019). [doi:10.3390/cancers11050688](https://doi.org/10.3390/cancers11050688) [Medline](#)
2. A. M. Pedley, S. J. Benkovic, A New View into the Regulation of Purine Metabolism: The Purinosome. *Trends Biochem. Sci.* **42**, 141–154 (2017). [doi:10.1016/j.tibs.2016.09.009](https://doi.org/10.1016/j.tibs.2016.09.009) [Medline](#)
3. J. M. Buchanan, S. C. Hartman, in *Advances in Enzymology and Related Areas of Molecular Biology, Vol. 21*, F. F. Nord, Ed. (Wiley, 1959), pp. 199–261.
4. S. C. Hartman, J. M. Buchanan, Nucleic acids, purines, pyrimidines (nucleotide synthesis). *Annu. Rev. Biochem.* **28**, 365–410 (1959). [doi:10.1146/annurev.bi.28.070159.002053](https://doi.org/10.1146/annurev.bi.28.070159.002053) [Medline](#)
5. G. R. Greenberg, L. Jaenicke, in *CIBA Foundation Symposium on the Chemistry and Biology Of Purines*, G. E. W. Wolstenholme, C. M. O'Connor, Eds. (Wiley, 1957), pp. 204–232.
6. S. An, R. Kumar, E. D. Sheets, S. J. Benkovic, Reversible compartmentalization of de novo purine biosynthetic complexes in living cells. *Science* **320**, 103–106 (2008). [doi:10.1126/science.1152241](https://doi.org/10.1126/science.1152241) [Medline](#)
7. H. Zhao, C. R. Chiaro, L. Zhang, P. B. Smith, C. Y. Chan, A. M. Pedley, R. J. Pugh, J. B. French, A. D. Patterson, S. J. Benkovic, Quantitative analysis of purine nucleotides indicates that purinosomes increase de novo purine biosynthesis. *J. Biol. Chem.* **290**, 6705–6713 (2015). [doi:10.1074/jbc.M114.628701](https://doi.org/10.1074/jbc.M114.628701) [Medline](#)
8. C. Y. Chan, H. Zhao, R. J. Pugh, A. M. Pedley, J. French, S. A. Jones, X. Zhuang, H. Jinnah, T. J. Huang, S. J. Benkovic, Purinosome formation as a function of the cell cycle. *Proc. Natl. Acad. Sci. U.S.A.* **112**, 1368–1373 (2015). [doi:10.1073/pnas.1423009112](https://doi.org/10.1073/pnas.1423009112) [Medline](#)
9. J. B. French, S. A. Jones, H. Deng, A. M. Pedley, D. Kim, C. Y. Chan, H. Hu, R. J. Pugh, H. Zhao, Y. Zhang, T. J. Huang, Y. Fang, X. Zhuang, S. J. Benkovic, Spatial colocalization and functional link of purinosomes with mitochondria. *Science* **351**, 733–737 (2016). [doi:10.1126/science.aac6054](https://doi.org/10.1126/science.aac6054) [Medline](#)
10. C. Y. Chan, A. M. Pedley, D. Kim, C. Xia, X. Zhuang, S. J. Benkovic, Microtubule-directed transport of purine metabolons drives their cytosolic transit to mitochondria. *Proc. Natl. Acad. Sci. U.S.A.* **115**, 13009–13014 (2018). [doi:10.1073/pnas.1814042115](https://doi.org/10.1073/pnas.1814042115) [Medline](#)
11. M. Kyoung, S. J. Russell, C. L. Kohnhorst, N. N. Esemoto, S. An, Dynamic architecture of the purinosome involved in human de novo purine biosynthesis. *Biochemistry* **54**, 870–880 (2015). [doi:10.1021/bi501480d](https://doi.org/10.1021/bi501480d) [Medline](#)

12. Y. Deng, J. Gam, J. B. French, H. Zhao, S. An, S. J. Benkovic, Mapping protein-protein proximity in the purinosome. *J. Biol. Chem.* **287**, 36201–36207 (2012).  
[doi:10.1074/jbc.M112.407056](https://doi.org/10.1074/jbc.M112.407056) [Medline](#)
13. M. Yang, K. H. Vousden, Serine and one-carbon metabolism in cancer. *Nat. Rev. Cancer* **16**, 650–662 (2016). [doi:10.1038/nrc.2016.81](https://doi.org/10.1038/nrc.2016.81) [Medline](#)
14. N. Kory, G. A. Wyant, G. Prakash, J. Uit de Bos, F. Bottanelli, M. E. Pacold, S. H. Chan, C. A. Lewis, T. Wang, H. R. Keys, Y. E. Guo, D. M. Sabatini, SFXN1 is a mitochondrial serine transporter required for one-carbon metabolism. *Science* **362**, eaat9528 (2018).  
[doi:10.1126/science.aat9528](https://doi.org/10.1126/science.aat9528) [Medline](#)
15. G. S. Ducker, J. D. Rabinowitz, One-Carbon Metabolism in Health and Disease. *Cell Metab.* **25**, 27–42 (2017). [doi:10.1016/j.cmet.2016.08.009](https://doi.org/10.1016/j.cmet.2016.08.009) [Medline](#)
16. M. D. Sintchak, M. A. Fleming, O. Futer, S. A. Raybuck, S. P. Chambers, P. R. Caron, M. A. Murcko, K. P. Wilson, Structure and mechanism of inosine monophosphate dehydrogenase in complex with the immunosuppressant mycophenolic acid. *Cell* **85**, 921–930 (1996). [doi:10.1016/S0092-8674\(00\)81275-1](https://doi.org/10.1016/S0092-8674(00)81275-1) [Medline](#)
17. C. F. Labuschagne, N. J. van den Broek, G. M. Mackay, K. H. Vousden, O. D. Maddocks, Serine, but not glycine, supports one-carbon metabolism and proliferation of cancer cells. *Cell Rep.* **7**, 1248–1258 (2014). [doi:10.1016/j.celrep.2014.04.045](https://doi.org/10.1016/j.celrep.2014.04.045) [Medline](#)
18. R. Nilsson, M. Jain, N. Madhusudhan, N. G. Sheppard, L. Strittmatter, C. Kampf, J. Huang, A. Asplund, V. K. Mootha, Metabolic enzyme expression highlights a key role for MTHFD2 and the mitochondrial folate pathway in cancer. *Nat. Commun.* **5**, 3128 (2014).  
[doi:10.1038/ncomms4128](https://doi.org/10.1038/ncomms4128) [Medline](#)
19. J. C. Venter, M. D. Adams, E. W. Myers, P. W. Li, R. J. Mural, G. G. Sutton, H. O. Smith, M. Yandell, C. A. Evans, R. A. Holt, J. D. Gocayne, P. Amanatides, R. M. Ballew, D. H. Huson, J. R. Wortman, Q. Zhang, C. D. Kodira, X. H. Zheng, L. Chen, M. Skupski, G. Subramanian, P. D. Thomas, J. Zhang, G. L. Gabor Miklos, C. Nelson, S. Broder, A. G. Clark, J. Nadeau, V. A. McKusick, N. Zinder, A. J. Levine, R. J. Roberts, M. Simon, C. Slayman, M. Hunkapiller, R. Bolanos, A. Delcher, I. Dew, D. Fasulo, M. Flanigan, L. Florea, A. Halpern, S. Hannenhalli, S. Kravitz, S. Levy, C. Mobarry, K. Reinert, K. Remington, J. Abu-Threideh, E. Beasley, K. Biddick, V. Bonazzi, R. Brandon, M. Cargill, I. Chandramouliswaran, R. Charlab, K. Chaturvedi, Z. Deng, V. Di Francesco, P. Dunn, K. Eilbeck, C. Evangelista, A. E. Gabrielian, W. Gan, W. Ge, F. Gong, Z. Gu, P. Guan, T. J. Heiman, M. E. Higgins, R.-R. Ji, Z. Ke, K. A. Ketchum, Z. Lai, Y. Lei, Z. Li, J. Li, Y. Liang, X. Lin, F. Lu, G. V. Merkulov, N. Milshina, H. M. Moore, A. K. Naik, V. A. Narayan, B. Neelam, D. Nusskern, D. B. Rusch, S. Salzberg, W. Shao, B. Shue, J. Sun, Z. Wang, A. Wang, X. Wang, J. Wang, M. Wei, R. Wides, C. Xiao, C. Yan, A. Yao, J. Ye, M. Zhan, W. Zhang, H. Zhang, Q. Zhao, L. Zheng, F. Zhong, W. Zhong, S. Zhu, S. Zhao, D. Gilbert, S. Baumhueter, G. Spier, C. Carter, A. Cravchik, T. Woodage, F. Ali,

- H. An, A. Awe, D. Baldwin, H. Baden, M. Barnstead, I. Barrow, K. Beeson, D. Busam, A. Carver, A. Center, M. L. Cheng, L. Curry, S. Danaher, L. Davenport, R. Desilets, S. Dietz, K. Dodson, L. Doup, S. Ferreira, N. Garg, A. Gluecksmann, B. Hart, J. Haynes, C. Haynes, C. Heiner, S. Hladun, D. Hostin, J. Houck, T. Howland, C. Ibegwam, J. Johnson, F. Kalush, L. Kline, S. Koduru, A. Love, F. Mann, D. May, S. McCawley, T. McIntosh, I. McMullen, M. Moy, L. Moy, B. Murphy, K. Nelson, C. Pfannkoch, E. Pratts, V. Puri, H. Qureshi, M. Reardon, R. Rodriguez, Y.-H. Rogers, D. Romblad, B. Ruhfel, R. Scott, C. Sitter, M. Smallwood, E. Stewart, R. Strong, E. Suh, R. Thomas, N. N. Tint, S. Tse, C. Vech, G. Wang, J. Wetter, S. Williams, M. Williams, S. Windsor, E. Winn-Deen, K. Wolfe, J. Zaveri, K. Zaveri, J. F. Abril, R. Guigó, M. J. Campbell, K. V. Sjolander, B. Karlak, A. Kejariwal, H. Mi, B. Lazareva, T. Hatton, A. Narechania, K. Diemer, A. Muruganujan, N. Guo, S. Sato, V. Bafna, S. Istrail, R. Lippert, R. Schwartz, B. Walenz, S. Yooseph, D. Allen, A. Basu, J. Baxendale, L. Blick, M. Caminha, J. Carnes-Stine, P. Caulk, Y.-H. Chiang, M. Coyne, C. Dahlke, A. Mays, M. Dombroski, M. Donnelly, D. Ely, S. Esparham, C. Fosler, H. Gire, S. Glanowski, K. Glasser, A. Glodek, M. Gorokhov, K. Graham, B. Gropman, M. Harris, J. Heil, S. Henderson, J. Hoover, D. Jennings, C. Jordan, J. Jordan, J. Kasha, L. Kagan, C. Kraft, A. Levitsky, M. Lewis, X. Liu, J. Lopez, D. Ma, W. Majoros, J. McDaniel, S. Murphy, M. Newman, T. Nguyen, N. Nguyen, M. Nodell, S. Pan, J. Peck, M. Peterson, W. Rowe, R. Sanders, J. Scott, M. Simpson, T. Smith, A. Sprague, T. Stockwell, R. Turner, E. Venter, M. Wang, M. Wen, D. Wu, M. Wu, A. Xia, A. Zandieh, X. Zhu, The sequence of the human genome. *Science* **291**, 1304–1351 (2001). [doi:10.1126/science.1058040](https://doi.org/10.1126/science.1058040) [Medline](#)
20. N. Winograd, Gas Cluster Ion Beams for Secondary Ion Mass Spectrometry. *Annu. Rev. Anal. Chem.* **11**, 29–48 (2018). [doi:10.1146/annurev-anchem-061516-045249](https://doi.org/10.1146/annurev-anchem-061516-045249) [Medline](#)
21. S. Fearn, Characterisation of biological material with ToF-SIMS: A review. *Mater. Sci. Technol.* **31**, 148–161 (2015). [doi:10.1179/1743284714Y.0000000668](https://doi.org/10.1179/1743284714Y.0000000668)
22. S. G. Boxer, M. L. Kraft, P. K. Weber, Advances in imaging secondary ion mass spectrometry for biological samples. *Annu. Rev. Biophys.* **38**, 53–74 (2009). [doi:10.1146/annurev.biophys.050708.133634](https://doi.org/10.1146/annurev.biophys.050708.133634) [Medline](#)
23. J. S. Fletcher, J. C. Vickerman, N. Winograd, Label free biochemical 2D and 3D imaging using secondary ion mass spectrometry. *Curr. Opin. Chem. Biol.* **15**, 733–740 (2011). [doi:10.1016/j.cbpa.2011.05.016](https://doi.org/10.1016/j.cbpa.2011.05.016) [Medline](#)
24. H. Tian, L. J. Sparvero, P. Blenkinsopp, A. A. Amoscato, S. C. Watkins, H. Bayır, V. E. Kagan, N. Winograd, Secondary-Ion Mass Spectrometry Images Cardiolipins and Phosphatidylethanolamines at the Subcellular Level. *Angew. Chem. Int. Ed.* **58**, 3156–3161 (2019). [doi:10.1002/ange.201814256](https://doi.org/10.1002/ange.201814256) [Medline](#)

25. T. B. Angerer, P. Blenkinsopp, J. S. Fletcher, High energy gas cluster ions for organic and biological analysis by time-of-flight secondary ion mass spectrometry. *Int. J. Mass Spectrom.* **377**, 591–598 (2015). [doi:10.1016/j.ijms.2014.05.015](https://doi.org/10.1016/j.ijms.2014.05.015)
26. S. Rabbani, A. M. Barber, J. S. Fletcher, N. P. Lockyer, J. C. Vickerman, TOF-SIMS with argon gas cluster ion beams: A comparison with C60+. *Anal. Chem.* **83**, 3793–3800 (2011). [doi:10.1021/ac200288v](https://doi.org/10.1021/ac200288v) [Medline](#)
27. J. S. Fletcher, S. Rabbani, A. Henderson, P. Blenkinsopp, S. P. Thompson, N. P. Lockyer, J. C. Vickerman, A new dynamic in mass spectral imaging of single biological cells. *Anal. Chem.* **80**, 9058–9064 (2008). [doi:10.1021/ac8015278](https://doi.org/10.1021/ac8015278) [Medline](#)
28. M. K. Passarelli, A. G. Ewing, Single-cell imaging mass spectrometry. *Curr. Opin. Chem. Biol.* **17**, 854–859 (2013). [doi:10.1016/j.cbpa.2013.07.017](https://doi.org/10.1016/j.cbpa.2013.07.017) [Medline](#)
29. H. Tian, L. J. Sparvero, A. A. Amoscato, A. Bloom, H. Bayır, V. E. Kagan, N. Winograd, Gas Cluster Ion Beam Time-of-Flight Secondary Ion Mass Spectrometry High-Resolution Imaging of Cardiolipin Speciation in the Brain: Identification of Molecular Losses after Traumatic Injury. *Anal. Chem.* **89**, 4611–4619 (2017). [doi:10.1021/acs.analchem.7b00164](https://doi.org/10.1021/acs.analchem.7b00164) [Medline](#)
30. V. Baresova, M. Krijt, V. Skopova, O. Souckova, S. Kmoch, M. Zikanova, CRISPR-Cas9 induced mutations along de novo purine synthesis in HeLa cells result in accumulation of individual enzyme substrates and affect purinosome formation. *Mol. Genet. Metab.* **119**, 270–277 (2016). [doi:10.1016/j.ymgme.2016.08.004](https://doi.org/10.1016/j.ymgme.2016.08.004) [Medline](#)
31. L. J. Sweetlove, A. R. Fernie, The role of dynamic enzyme assemblies and substrate channelling in metabolic regulation. *Nat. Commun.* **9**, 2136 (2018). [doi:10.1038/s41467-018-04543-8](https://doi.org/10.1038/s41467-018-04543-8) [Medline](#)
32. V. Pareek *et al.*, Penn State ScholarSphere (2020); <https://doi.org/10.26207/8rm3-g809>.
33. A. S. Tibbetts, D. R. Appling, Compartmentalization of Mammalian folate-mediated one-carbon metabolism. *Annu. Rev. Nutr.* **30**, 57–81 (2010). [doi:10.1146/annurev.nutr.012809.104810](https://doi.org/10.1146/annurev.nutr.012809.104810) [Medline](#)
34. A. Misak, M. Grman, L. Malekova, M. Novotova, J. Markova, O. Krizanova, K. Ondrias, Z. Tomaskova, Mitochondrial chloride channels: Electrophysiological characterization and pH induction of channel pore dilation. *Eur. Biophys. J.* **42**, 709–720 (2013). [doi:10.1007/s00249-013-0920-2](https://doi.org/10.1007/s00249-013-0920-2) [Medline](#)
35. L. B. Sullivan, D. Y. Gui, A. M. Hosios, L. N. Bush, E. Freinkman, M. G. Vander Heiden, Supporting Aspartate Biosynthesis Is an Essential Function of Respiration in Proliferating Cells. *Cell* **162**, 552–563 (2015). [doi:10.1016/j.cell.2015.07.017](https://doi.org/10.1016/j.cell.2015.07.017) [Medline](#)

36. N. D. Amoedo, G. Punzi, E. Obre, D. Lacombe, A. De Grassi, C. L. Pierri, R. Rossignol, AGC1/2, the mitochondrial aspartate-glutamate carriers. *Biochim. Biophys. Acta* **1863**, 2394–2412 (2016). [doi:10.1016/j.bbamcr.2016.04.011](https://doi.org/10.1016/j.bbamcr.2016.04.011) [Medline](#)
37. W. Lu, M. F. Clasquin, E. Melamud, D. Amador-Noguez, A. A. Caudy, J. D. Rabinowitz, Metabolomic analysis via reversed-phase ion-pairing liquid chromatography coupled to a stand alone orbitrap mass spectrometer. *Anal. Chem.* **82**, 3212–3221 (2010). [doi:10.1021/ac902837x](https://doi.org/10.1021/ac902837x) [Medline](#)
38. L. Hedstrom, IMP dehydrogenase: Structure, mechanism, and inhibition. *Chem. Rev.* **109**, 2903–2928 (2009). [doi:10.1021/cr900021w](https://doi.org/10.1021/cr900021w) [Medline](#)
39. H. Tian, D. A. Six, T. Krucker, J. A. Leeds, N. Winograd, Subcellular Chemical Imaging of Antibiotics in Single Bacteria Using C<sub>60</sub>-Secondary Ion Mass Spectrometry. *Anal. Chem.* **89**, 5050–5057 (2017). [doi:10.1021/acs.analchem.7b00466](https://doi.org/10.1021/acs.analchem.7b00466) [Medline](#)
40. S. An, Y. Deng, J. W. Tomsho, M. Kyoung, S. J. Benkovic, Microtubule-assisted mechanism for functional metabolic macromolecular complex formation. *Proc. Natl. Acad. Sci. U.S.A.* **107**, 12872–12876 (2010). [doi:10.1073/pnas.1008451107](https://doi.org/10.1073/pnas.1008451107) [Medline](#)
41. T. T. Puck, P. I. Marcus, S. J. Cieciera, Clonal growth of mammalian cells in vitro; growth characteristics of colonies from single HeLa cells with and without a feeder layer. *J. Exp. Med.* **103**, 273–283 (1956). [doi:10.1084/jem.103.2.273](https://doi.org/10.1084/jem.103.2.273) [Medline](#)